Thesis for the Degree of Licentiate of Engineering

Disruption Mitigation in Tokamaks with Massive Material Injection

OSKAR VALLHAGEN

Department of Physics
CHALMERS UNIVERSITY OF TECHNOLOGY
Göteborg, Sweden 2023

Disruption Mitigation in Tokamaks with Massive Material Injection
OSKAR VALLHAGEN

Division of Subatomic, High Energy and Plasma Physics
Department of Physics
Chalmers University of Technology
SE-412 96 Göteborg
Sweden
Telephone: +46 (0)31 772 1000

Cover:
Contour plots of the deuterium density at different times during shattered pellet injection in a circular cross-section tokamak plasma, simulated with DREAM. The color scale ranges from 10^{20} m^{-3} (black) to $7 \cdot 10^{21}$ m^{-3} (white). The pellet shard positions are marked by cyan dots, whose sizes are proportional to the shard radii.

Typeset in LaTeX
Printed in Sweden by
Chalmers digitaltryck
Göteborg, Sweden 2023

Disruption Mitigation in Tokamaks with Massive Material Injection

OSKAR VALLHAGEN

Department of Physics
Chalmers University of Technology

Abstract

The sudden loss of confinement of the energy content of fusion plasmas in off-normal events, called disruptions, is among the most severe threats to the future of fusion energy based on the tokamak design. An efficient disruption mitigation system will therefore be of utmost importance for future large, high-current devices such as ITER. The potentially greatest threat to be mitigated is posed by currents carried by highly energetic electrons, called runaway electrons, which may cause severe damage upon wall impact. The disruption mitigation system must also ensure a sufficiently homogeneous deposition of the thermal energy on the plasma-facing components, and avoid excessive forces on the machine due to currents flowing in the surrounding structures. The currently envisaged mitigation method is to initiate a massive material injection, e.g. in the form of a pressurized gas or a shattered cryogenic pellet, when an emerging disruption is detected, and so attempt to better control the plasma cooling and energy dissipation.

In this thesis, we develop modeling tools for the various physical phenomena present during a tokamak disruption mitigated by a massive material injection. This includes extending the numerical tools GO and DREAM with the capability to handle more advanced geometry, effects of partial ionization in the cooling plasma on the generation of runaway electrons, and the material assimilation in the plasma following a shattered pellet injection. These tools are then used to perform integrated numerical simulations, assessing the mitigation performance for a wide range of injection scenarios in reactor-scale tokamak devices. Finally, we also develop an analytical model for the radial transport of the relatively cold and dense material recently ablated from a shattered pellet upon exposure to the hot plasma.

Our results indicate that the severity of a disruption in a reactor-scale device can be significantly reduced by a carefully chosen injection scheme and composition of the injected material. In particular, a two-stage shattered pellet injection might efficiently reduce the localised heat loads and the runaway generation due to the hot-tail mechanism, by allowing for an intermediate equilibration of the superthermal electron population between the injections. However, the strong runaway avalanche associated with a high plasma current was found to be able to amplify even a very small runaway seed, such as those produced by tritium decay and Compton scattering during nuclear operation, to several mega-amperes. The reason is that the intense cooling from the injected material leads to a high induced electric field and a substantial recombination, resulting in an enhanced avalanche multiplication. Our calculations also indicate that this mitigation scheme might be further complicated by a relatively large outward drift of the recently ablated pellet material.

Keywords: fusion plasma, disruption mitigation, shattered pellet injection, runaway electron

List of publications

A Fülöp, T., Helander, P., Vallhagen, O., Embreus, O., Hesslow, L., Svensson, P., Creely, A. J., Howard, N. T. & Rodriguez-Fernandez, P. 2020 "Effect of plasma elongation on current dynamics during tokamak disruptions". *Journal of Plasma Physics* **86**, 474860101,
doi: 10.1017/S002237782000001X

B Vallhagen, O., Embreus, O., Pusztai, I., Hesslow, L. & Fülöp, T. 2020 "Runaway dynamics in the DT phase of ITER operations in the presence of massive material injection". *Journal of Plasma Physics* **86**, 475860401,
doi: 10.1017/S0022377820000859

C Vallhagen, O., Pusztai, I., Hoppe, M., Newton, S. L. & Fülöp, T. 2022 "Effect of two-stage shattered pellet injection on tokamak disruptions". *Nuclear Fusion* **62**, 112004,
doi: 10.1088/1741-4326/ac667e

D Vallhagen, O., Pusztai, I., Helander, P., Newton, S. L. & Fülöp, T. 2023 "Drift of ablated material after pellet injection in a tokamak". Submitted to: *Journal of Plasma Physics*
https://arxiv.org/abs/2301.12911

Related publications, not included in the thesis

E Hesslow, L., Embreus, O., Vallhagen, O. & Fülöp, T. 2019 "Influence of massive material injection on avalanche runaway generation during tokamak disruptions". *Nuclear Fusion* **59**, 084004,
doi: 10.1088/1741-4326/ab26c2

F Hesslow, L., Unnerfelt, L., Vallhagen, O., Embreus, O., Hoppe, M., Papp, G., & Fülöp, T. 2019 "Evaluation of the Dreicer runaway growth rate in the presence of high-Z impurities using a neural network". *Journal of Plasma Physics* **85**, 475850601,
doi: 10.1017/S0022377819000874

G Insulander Björk, K., Papp, G., Embreus, O., Hesslow, L., Fülöp, T., Vallhagen, O., Lier, A., Pautasso, G., Bock, A., the ASDEX Upgrade team & the EUROfusion MST1 team 2020 "Kinetic modelling of runaway electron generation in argon-induced disruptions in ASDEX Upgrade". *Journal of Plasma Physics* **86**, 855860401,
doi: 10.1017/S0022377820000793

H Creely, A. J., Greenwald, M. J., Ballinger, S. B., Brunner, D., Canik, J., Doody, J., Fülöp, T., Garnier, D. T., Granetz, R., Gray, T. K., Holland, C., Howard, N. T., Hughes, J. W., Irby, J. H., Izzo, V. A., Kramer, G. J., Kuang, A. Q., LaBombard, B., Lin, Y., Lipschultz, B., Logan, N. C., Lore, J. D., Marmar, E. S., Montes, K., Mumgaard, R. T., Paz-Soldan, C., Rea, C., Reinke, M. L., Rodriguez-Fernandez, P., Särkimäki, K., Sciortino, F., Scott, S. D., Snicker, A., Snyder, P. B., Sorbom, B. N., Sweeney, R., Tinguely, R. A., Tolman, E. A., Umansky, M., Vallhagen, O., Varje, J., Whyte, D. G., Wright, J. C., Wukitch, S. J., Zhu, J. & the SPARC Team 2020 "Overview of the SPARC tokamak". *Journal of Plasma Physics* **86**, 865860502,
doi: 10.1017/S0022377820001257

I Sweeney, R., Creely, A. J., Doody, J., Fülöp, T., Garnier, D. T., Granetz, R., Greenwald, M., Hesslow, L., Irby, J., Izzo, V. A., La Haye, R. J., Logan, N. C., Montes, K., Paz-Soldan, C., Rea, C., Tinguely, R. A., Vallhagen, O. & Zhu, J. 2020 "MHD stability and disruptions in the SPARC tokamak". *Journal of Plasma Physics* **86**, 865860507,
doi: 10.1017/S0022377820001129

J Svensson, P., Embreus, O., Newton, S. L., Särkimäki, K., Vallhagen, O. & Fülöp, T. 2021 "Effects of magnetic perturbations and radiation on the runaway avalanche". *Journal of Plasma Physics* **87**, 905870207,
doi: 10.1017/S0022377820001592

K Insulander Björk, K., Vallhagen, O., Papp, G., Reux, C., Embreus, O., Rachlew, E., Fülöp, T., the ASDEX Upgrade team, JET contributors & the EUROfusion MST1 team 2021 "Modelling of runaway electron dynamics during argon-induced disruptions in ASDEX Upgrade and JET". *Plasma Physics and Controlled Fusion* **63**, 085021,
doi: 10.1088/1361-6587/ac07b5

L Pusztai, I., Hoppe, M. & Vallhagen, O. 2022 "Runaway dynamics in tokamak disruptions with current relaxation". *Journal of Plasma Physics* **88**, 905880409,
doi: 10.1017/S0022377822000733

M Berger, E., Pusztai, I., Newton, S. L., Hoppe, M., Vallhagen, O., Fil, A. & Fülöp, T. 2022 "Runaway dynamics in reactor-scale spherical tokamak disruptions". *Journal of Plasma Physics* **88**, 905880611,
doi: 10.1017/S0022377822001209

N Pusztai, I., Ekmark, I., Bergström, H., Halldestam, P., Jansson, P., Hoppe, M., Vallhagen, O. & Fülöp, T. 2023 "Bayesian optimization of massive material injection for disruption mitigation in tokamaks". *Journal of Plasma Physics* **89**, 905890204,
doi: 10.1017/S0022377823000193

Acknowledgments

I would like to express my sincerest gratitude towards all the people who have supported me in my early scientific career, leading up to the finishing of this thesis. First of all, I want to thank my main supervisor and mentor Tünde Fülöp, for giving me the life-changing opportunity to work with this group already since I was only a second-year Bachelor student. Her guidance and support has continuously made my performance greatly exceed my abilities. I have also received invaluable support from my co-supervisors István Pusztai and Sarah Newton, who always take their time to help with whatever I need, despite their busy schedules and my sometimes short notice and irregular response. I also want to thank my examiner Christian Forssén, for taking his time to be involved in my PhD studies although they are not related to his field.

The work in this thesis would not have been possible without the collaboration with several other colleagues. I especially want to thank Mathias Hoppe for making sure that I don't have to worry when my simulations crash, Lise Hanebring for the countless simulations I have not had to do on my own, and Per Helander for giving me the privilege of spending his valuable time and expertise on me. A substantial part of the work included in this thesis has also been made in collaboration with Linnea Hesslow and Ola Embreus; thank you for your great help with my research and learning curve within the field, I really miss working with you. The list could of course be extended to include all remaining past and present members of the group, nobody named, nobody forgotten.

Besides the academic community, I could not have finished this thesis without the support and presence from my great family and friends. A special thanks goes to Julia Järlebark and Erik Svensson, for always keeping in touch, making me feel welcome and caring about my problems, however severe or silly they might be. I also want to thank all past and present members of F-spexet, for the companionship and warm environment that really makes you feel like a weird second family. Finally, I want to thank my real family, for always being caring and supportive despite my recurring lack of time to return the favor; I hope I will have more time to do so after finishing this thesis.

Oskar Vallhagen, Göteborg, 2023-04-18

Contents

Chapter 1

Introduction

The steadily increasing energy consumption around the world will make future generations' demand for reliable and clean energy sources larger than ever before. If successful, fusion energy has the potential to play a key role in a future carbon-free energy system. Even if commercial fusion does not become available soon enough to tackle the most urgent climate changes, it may still be of importance to meet the increasing energy demand during the later half of this century (Cabal *et al.*, 2017).

In many ways, fusion can be regarded as an ideal energy source (Chen, 2011): The fusion reactions do not produce any other waste products than helium, making fusion sustainable from a climate perspective. The hydrogen isotopes used as fuel can be extracted from ordinary sea water or can be produced at the power plant through lithium breeding by neutron irradiation, making the fuel reserves practically unlimited. The energy production is not weather-dependent, and the fusion energy output can therefore be adapted to a varying demand to a greater extent than intermittent renewable energy sources. The half-life of the radioactive materials produced by neutron bombardment of the reactor wall is of the order of hundreds of years. This is about a thousand times shorter than the hundreds of thousands of years for some of the high level radioactive waste produced by a fission reactor. Finally, fusion produces no by-products that may be used for nuclear weapons.

There are, however, many difficulties involved in realizing a fusion power plant (Chen, 1974). In order to fuse two nuclei, the distance between them must be similar to their de Broglie wavelength. At this point, the probability to overcome the remaining Coulomb potential barrier by tunneling becomes significant. For this to happen, the nuclei have to overcome the Coulomb repulsion at larger distances, and therefore they have to collide at a very high energy. In order to achieve such energetic collisions, the fuel must be heated to a temperature of the order of 10^8 K. Confining such a hot fuel and maintaining the conditions necessary for a substantial fusion reaction rate is a challenging task. The most developed method to overcome these challenges, aiming to use fusion as an energy source, is so-called magnetically confined fusion, which is introduced in section 1.1.

Although magnetically confined fusion devices allow for a stable confinement of the fusion fuel during normal operation, they must also be able to handle off-normal events, where the confinement is suddenly lost, called disruptions (Hollmann *et al.*, 2015). These events result in a rapid release of the stored thermal and magnetic

energy, which can be very dangerous for the machine integrity. The basic features of disruptions, their consequences, and suggested methods to mitigate their impact on the machine are introduced in section 1.2. However, disruption mitigation in future large reactor-scale fusion devices is still an unresolved issue. This is the topic to which this thesis aims to contribute, by providing specific guidelines to mitigate the effects of such events.

1.1 Magnetic plasma confinement and the tokamak design

At the high temperatures necessary for fusion energy generation, the electrons in the fuel are separated from the atomic nuclei. When this happens, the fuel becomes a plasma, which may be regarded as a gas consisting of unbound charged particles. Since the particles are charged, they may be controlled by a magnetic field, which is the fundamental physical basis of magnetic confinement fusion.

When a charged particle is subject to a magnetic field, it undergoes gyro-motion around the magnetic field lines (Freidberg, 2008). Naively, one could therefore confine the plasma by bending the magnetic field into a torus. This is indeed the basic principle behind magnetically confined fusion. However, the construction of such a magnetic field inevitably introduces a gradient of the field strength along the major radius of the torus. This magnetic field gradient makes a plasma in a purely toroidal magnetic field intrinsically unstable, as explained below.

A gradient in the magnetic field makes the radius of the gyro-motion longer in the part of the gyration where the magnetic field is weaker, compared to the part where it is stronger. This results in a drift of the center of gyration, called the *guiding center*, perpendicular to both the magnetic field and its gradient, as illustrated in the left panel of figure 1.1. This drift is referred to as the ∇B*-drift*. As the ∇B-drift is oppositely directed for electrons and ions, it will induce a charge separation in the plasma, generating a vertical electric field.

This electric field also affects the gyro radius during the particle motion; When the particle moves in the same direction as the electric field, its speed, and therefore its gyro radius, increases, and when it moves in the direction opposite to the electric field it decreases. This causes the gyro radius to vary along the direction of the electric field, in opposing ways for electrons and ions, leading to a guiding center drift perpendicular to both the magnetic and electric field, as illustrated in the right panel of figure 1.1. This drift is referred to as the $E \times B$ *drift*. As evident from figure 1.1, this drift has the same direction for both electrons and ions, leading to the whole plasma drifting out of confinement.

This issue can be resolved by introducing a poloidal twist to the magnetic field, i.e. a magnetic field component circulating the short way around the torus, as illustrated in the left panel of figure 1.2 (Freidberg, 2008). Such a twist makes the particles circulate around the plasma in the poloidal direction in a way that averages out the effect of the vertical ∇B-drift; in the upper part of the poloidal motion, the ∇B-drift drives the particles away from the plasma center, while in the lower part the ∇B-drift drives the particle back towards the center. Such a trajectory is

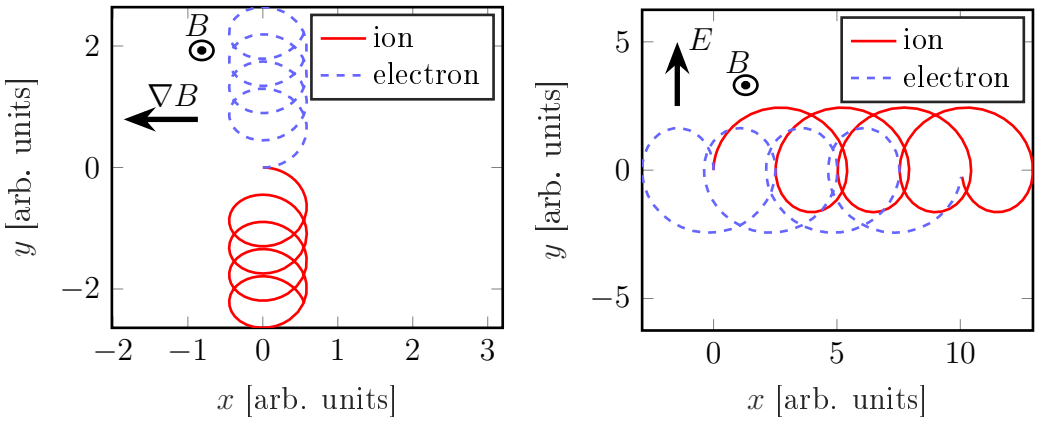

Figure 1.1: Particle trajectories for an ion and electron, starting from the origin, with different prescribed electric and magnetic field settings: (left) a magnetic field pointing in the positive z-direction (out from the paper) with a uniform gradient in the negative x-direction, giving rise to a ∇B-drift. The resulting charge separation gives rise to an electric field in the positive y-direction. (Right) a constant uniform magnetic field pointing in the positive z-direction and a constant uniform electric field pointing in the positive y-direction, giving rise to an $E \times B$-drift. Note that electrons and ions with comparable kinetic energy have disparate gyro-radii, however, here we depict their orbits with similar gyro-radii for visibility.

illustrated in the right panel of figure 1.2. In that way, the charge separation, and hence the $E \times B$-drift that would break the confinement, is avoided.

In the most studied design for such a configuration, the so-called *tokamak*, this twist of the field lines is achieved by driving a large toroidal current through the plasma, of the order of mega-amperes (MAs). In such a configuration, the magnetic field lines can be shown to circulate in the plasma following nested toroidal surfaces called *flux surfaces* (surfaces of constant poloidal magnetic flux), sketched in the left panel of figure 1.2 (Freidberg, 2008). The particles in the plasma then stay essentially confined to one of those flux surfaces*, as indicated in the right panel of figure 1.2.

The tokamak design is utilised by the JET (Joint European Torus) device, currently holding the record for the ratio of the generated fusion power to the supplied heating power - the so-called Q-factor - at 0.67. It is also used for future devices aiming at producing a net gain of fusion energy. These devices include SPARC, under development by Commonwealth Fusion Systems (Paper **H**), STEP (Spherical Tokamak for Energy Production) under development by the UK Atomic Energy Authority, and ITER, which is currently under construction in France by the ITER organization. ITER will be the largest among the next generation of fusion devices, and is the main concern of this thesis. The ITER project is an international collaboration between the European Union, United States, China, Russia, South Korea, India and Japan, aiming for a Q-factor of 10. In order to increase the Q-factor, next-generation devices will store significantly larger thermal and magnetic energies than current experiments. This increases the severity of the threat posed by disruptions,

*In the absence of fluctuations and collisions, which are important on a longer time scale.

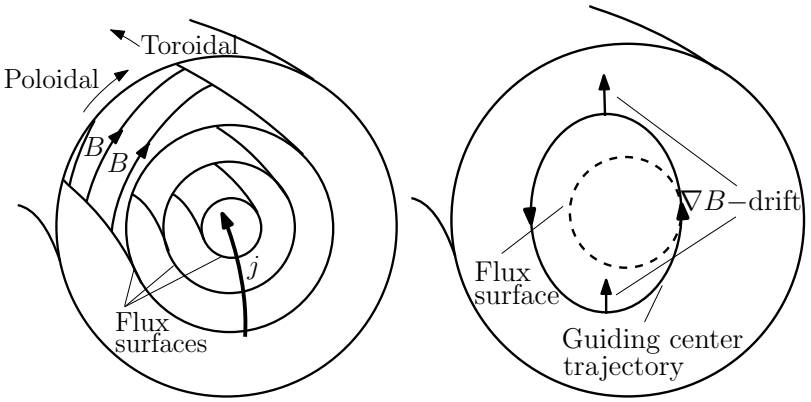

Figure 1.2: (Left) Illustration of the magnetic field configuration in a tokamak; the magnetic field is the sum of a toroidal component generated by external coils (not shown in the figure) and a poloidal component generated by the plasma current. The resulting magnetic field lines follow helical paths around the plasma, ordered in a set of nested flux surfaces. (Right) Projection of the guiding center trajectory of an ion in a tokamak on the poloidal plane, illustrating how the ∇B-drift is averaged out by the motion along the poloidal component of the magnetic field. A flux surface with circular cross section, tangential to the ion guiding center trajectory, is included as reference. The drift away from the flux surface is exaggerated for visibility.

to which we now turn our attention.

1.2 Tokamak disruptions

Disruptions are a form of operational failure, where the plasma confinement is suddenly lost, and the energy contained in the plasma is dissipated to the surrounding structures (Hender *et al.*, 2007). A disruption typically include three phases, as illustrated in figure 1.3. During the first phase of a disruption, called the *thermal quench* (indicated by red in figure 1.3), the vast majority of the thermal energy may be released over a time scale as short as 0.1–1 ms, and the temperature typically drops by several orders of magnitude. This phase is usually triggered by a perturbation to the magnetic field that grows unstable, leading to the development of a so-called magnetohydrodynamic (MHD) instability. Such an instability introduces a stochastic component to the magnetic field which, to some extent, temporarily breaks the flux surface geometry and therefore strongly enhances the radial transport of particles and heat, until the flux surfaces re-heal as the thermal quench approaches its end. The triggering perturbation might be caused by e.g. an influx of impurities, either originating from the wall or injected deliberately in an attempt to control the plasma cooling as discussed below, in which cases line radiation and bremsstrahlung due to the impurities also contribute to the thermal energy loss.

The drop in temperature also comes with a drop in conductivity, leading to dissipation of the magnetic energy associated with the plasma current. This drop in conductivity can be understood by considering that, in a plasma, the collisional interaction between the particles is dominated by the their Coulomb interaction (Chen, 1974). This leads to the somewhat counter-intuitive phenomenon that the

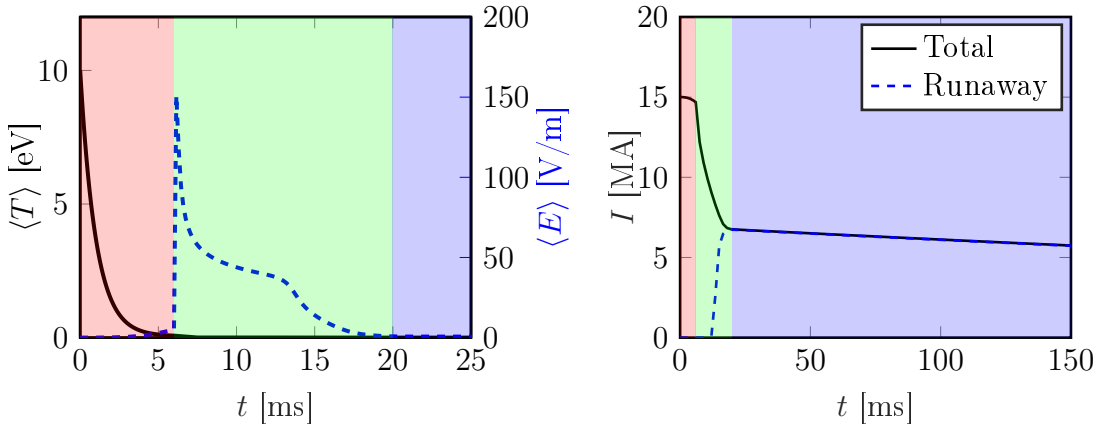

Figure 1.3: Illustration of the general features of a disruption, based on a disruption simulation in an ITER-like plasma (corresponding to Case 1 in paper **B**). The panels show (left) the average temperature drop and resulting increase and decay of the average electric field, and (right) the current decay. The shaded areas indicate the time spans of the thermal quench (red), current quench (green), and runaway plateau (blue), respectively.

drag force felt by a particle moving through the plasma decreases with the particle momentum, as particles with a higher relative momentum spend less time in the vicinity of one another, giving the Coulomb force less time to cause a momentum change. The conductivity is inversely proportional to the drag force between electrons and ions, which have a typical relative speed dominated by the electron thermal motion, and therefore a drop in temperature results in a drop in the conductivity. The phase of the disruption thus initiated, indicated by green in figure 1.3, is called the *current quench*, and has a time scale 1–2 orders of magnitude longer than the thermal quench, depending on the size and operation parameters of the tokamak.

The rapid release of the thermal and magnetic energy might cause severe damage to the device (Hollmann *et al.* (2015), Paper **I**). The rapid release of the thermal energy can cause a substantial sputtering, or even melting, of the wall material. A rapid current drop can induce large eddy currents in the structures surrounding the plasma, which in the presence of the strong magnetic fields used to control the plasma may result in large forces being exerted on the machine. Conversely, if the current decay is slow, the plasma control might be lost while there is a substantial current remaining in the plasma. The currents in the outer layers of the plasma may then begin to flow through the surrounding structures, forming a so-called halo-current. Such a current may also lead to large forces being exerted on the machine.

Finally, the potentially most severe threat to a reactor-scale tokamak is the generation of extremely energetic electrons, called runaway electrons (Hollmann *et al.*, 2015). These electrons may cause a significant melting of plasma-facing compnents upon impact. Their existence is made possible by the momentum dependence of the drag force felt by a charged particle moving through the plasma mentioned above, together with the induction of a large electric field in the plasma during the disruption. The decrease in the drag force at high momenta allows the force exerted by an

electric field to overcome the drag force for particles with a momentum higher than a critical value, enabling these particles to be accelerated to extremely high energies. An electric field must be induced during the fast temperature drop to compensate for the associated drop in the conductivity, as the inductive properties of the system, including the metallic vacuum vessel containing the plasma, set a lower limit on the time scale over which the current can change. This electric field might be strong enough to enable the existence of runaway electrons.

As long as there is any mechanism present which can feed the region of momentum space above the critical momentum, as described in section 2.2.2, a part of the plasma current will be replaced by a runaway current which, due to the low collisionality at high momenta, can remain for a relatively long time, even after the electric field has decayed. This phase of the disruption, indicated by blue in figure 1.3, is called the *runaway plateau phase*, and typically lasts until the vertical control is lost and the runaway current impacts the wall.

The potential damage resulting from a disruption described above poses strict requirements for disruption mitigation (Hollmann *et al.*, 2015). Three main tasks must be accomplished by a tokamak disruption mitigation system. The first is to minimize the localized heat loads on the plasma facing components, by spreading the heat loads over as large an area as possible. Secondly, the disruption mitigation system must control the time scale for the current decay so that it is long enough to avoid excessive eddy currents, but short enough to avoid excessive halo currents. Finally, the current carried by runaway electrons impacting the wall should be minimized.

The currently envisaged disruption mitigation method is to inject a comparatively massive amount of material into the plasma as soon as the emerging disruption is detected. The injection primarily consists of hydrogen isotopes and/or noble gases, such as neon or argon. As this material enters the plasma in the form of neutral atoms, and typically remains not fully ionized for a substantial part of the disruption, it may emit line radiation when excited by exposure to the plasma. This radiation can release the thermal energy isotropically, reducing the maximum localised heat loads. The amount and composition of the injected material can also be tuned to gain some control over the temperature after the initial drop, which in turn determines the current decay rate. Moreover, as the injected material ionizes, the electron density increases. This leads to an increase in the drag force felt by the electrons in the plasma, which to some extent can be used to reduce the runaway generation. However, if the injected quantities are too large, the resulting cooling might be intense enough to cause a substantial recombination, in which case this mitigation mechanism might not be successful anymore (see section 2.2.2 and paper **B**).

Conventionally, the injected material is delivered as a gas puff from a pressurized vault (Hollmann *et al.*, 2015). While this technique is comparatively simple, it comes with a number of disadvantages. The injected gas ionizes rapidly when exposed to the still hot plasma. When ionized, the injected material becomes tied to the magnetic field, which substantially slows down the transport towards the plasma core. Moreover, the gas injection introduces a perturbation to the magnetic field, which accelerates the growth of the plasma instabilities. As a result, the disruption

might fully begin before the injected material has reached the plasma center.

Another approach, that can provide better core penetration, is to inject material in the form of a solid, cryogenic pellet. The exposure to the plasma causes the pellet to ablate and deposit its content along its trajectory. The ablation can be made more efficient by shattering the pellet into smaller shards before it enters the plasma, forming a so-called Shattered Pellet Injection (SPI). This technique has been chosen as the baseline for the disruption mitigation system at ITER (Lehnen *et al.*, 2020). There are however potential drawbacks of this technique as well. One important example stems from the fact that in the very dense plasma cloud surrounding the ablating pellet, the poloidal component of the magnetic field cannot average out the local ∇B-drift, so that a local charge separation occurs. The corresponding $E \times B$-drift will transport the ablated material along the major radius direction until it has homogenized with the rest of the plasma, which lowers the core penetration and might even expel the ablated material from the plasma. In conclusion, the design of a disruption mitigation system for a reactor-scale tokamak remains an open question, to which the work in this thesis aims to contribute.

1.3 Thesis outline

The rest of this thesis is structured as follows. In chapter 2 the theory governing the momentum space dynamics in a plasma is introduced, with a focus on the formation of runaway electrons. Chapter 3 gives an overview of different disruption mitigation strategies, as well as the physics of pellet injection in a tokamak, which is the injection technique most thoroughly studied in this work. The components necessary for a full disruption mitigation model are then summarized in chapter 4, and the numerical tools GO and DREAM, which are used extensively in this work, are introduced. Finally, the appended papers are summarized in chapter 5, where we also discuss the implications of this work and suggestions for future studies.

Chapter 2

Momentum space dynamics of plasmas

Many of the phenomena at play during a tokamak disruption introduced in the previous chapter are related to the way the electron phase space distribution function evolves in a plasma and how it couples to the electromagnetic fields present. More precisely, the collisional properties of a plasma play a particularly important role. In this chapter we start by giving a qualitative illustration of the collisional dynamics of a plasma in section 2.1, where we also derive scaling laws providing an intuitive understanding of the electrical conductivity and the runaway phenomenon in a plasma. We then give a brief overview of the so-called kinetic equation, which governs the electron phase space distribution function in a plasma, in section 2.2, before taking a more detailed look at the runaway phenomenon and how runaway electrons are generated in a tokamak disruption in section 2.2.2.

2.1 Coulomb collisions

Collisions in a plasma differ quite significantly from collisions in a gas. Instead of the binary close collisions dominating in a gas, the collisional dynamics in a plasma is dominated by long-range interactions through the Coulomb force. An important consequence of this is that, as we will see shortly, fast particles are *less* collisional than slow particles, as opposed to the case in a gas.

A qualitative comparison of the difference between Coulomb collisions and close collisions prevailing in a gas is illustrated in the left panel of figure 2.1. This illustration is made using a simple simulation of a particle traveling through a fixed ion background (corresponding to background particles with a much larger mass than the test particle, which would be the case if the moving particle was an electron). If the particle is neutral, so that the interaction with the background takes place through close collisions, the resulting trajectory will be made up of straight line segments with sharp deflections where a collision takes place. If the particle is an electron, on the other hand, the long-range Coulomb interaction with the background ions causes the electron to follow a smoothly curved path. Notably, while the path of the neutral particle is determined by a set of consecutive large angle collisions, the path of the electron is determined by the contribution from many

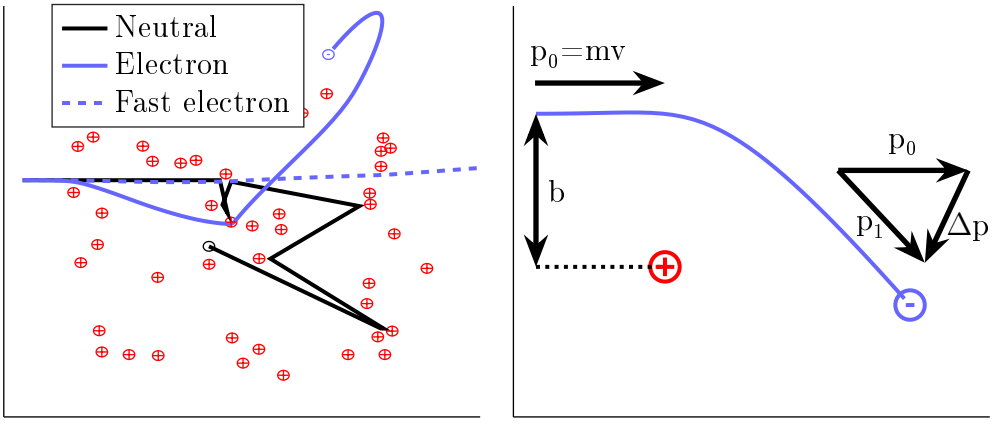

Figure 2.1: (Left) Illustration of a neutral atom (black), and two electrons (blue) with different speeds moving through a background of fixed ions, comparing electron-ion Coulomb collisions with close collisions with neutrals, and illustrating the velocity dependence of Coulomb collisions. (Right) Illustration of a single Coulomb collision between an incident electron and a fixed ion. Note that for the vast majority of collisions $\Delta p \ll p_0$, although Δp is exaggerated here for visibility.

small angle collisions with many ions at the same time (Helander & Sigmar, 2005). Moreover, for the neutral particle, the deflection angle is independent of the particle speed, but for the electron interacting through the Coulomb force, we see that a fast electron is significantly less affected by the background ions than a slower one. This happens because the time spent in the vicinity of the ions decreases with an increasing electron speed, without affecting the interaction force.

The setup for a single Coulomb collision of an electron with mass m, traveling with a velocity v and colliding with a fixed ion is shown in the right panel of figure 2.1. The ion is assumed here to have an equal but opposite charge compared to the electron. In the absence of the Coulomb force, the electron would have a distance of closest approach equal to b as defined in the figure, which is referred to as the *impact parameter*. After the collision, the electron has acquired a change in momentum of magnitude Δp.

Before turning to a rigorous kinetic description of Coulomb collisions, one may gain an increased intuitive understanding based on scaling laws derived from the simple case depicted above. The velocity scaling of the cross section and collision frequency of electron-ion Coulomb collisions, defined as the rate at which the electron momentum undergoes an order unity relative change, can be determined as follows. As mentioned above, for Coulomb collisions, the momentum change is dominated by the accumulated effect of many small-angle interactions, but as we are primarily interested in the speed scaling here, we may simplify the picture by considering events where the order unity momentum change occurs due to a single Coulomb interaction. During the main part of this interaction, the Coulomb force is roughly given by

$$F_\mathrm{c} \sim \frac{e^2}{4\pi\epsilon_0 b^2}, \tag{2.1}$$

where e is the elementary charge and ϵ_0 is the vacuum permittivity, and is felt during

a collision duration time roughly given by $t_c \sim b/v$. From these considerations, we may relate the impact parameter necessary for a significant deflection of the electron to the electron velocity according to

$$\Delta p \sim mv \sim F_c t_c \sim \frac{e^2}{4\pi\epsilon_0 bv} \Rightarrow b \sim \frac{e^2}{4\pi\epsilon_0 mv^2}. \tag{2.2}$$

The cross section can then be estimated according to

$$\sigma_c \sim \pi b^2 \sim \frac{e^4}{16\pi\epsilon_0^2 m^2 v^4}. \tag{2.3}$$

The collision frequency can now be estimated by the number of electrons passing through a cross section of area σ_c per unit time, according to

$$\nu \sim nv\sigma_c \sim \frac{ne^4}{16\pi\epsilon_0^2 m^2 v^3}. \tag{2.4}$$

Here, n is the density of electrons or ions, assumed to be equal here for simplicity. The important take-away here is the $1/v^3$-scaling, which quantifies the previous observation that fast particles are less collisional in a plasma. In practice, however, the particles in a plasma do not all have the same velocity, but usually a thermal, Maxwellian, distribution of velocities. To estimate the collision frequency for a thermal plasma, we may therefore replace the velocity v by the thermal speed $v_{\text{th}} = \sqrt{k_B T/m}$ and obtain the thermal collision frequency as

$$\nu_{\text{th}} = \frac{ne^4}{16\pi\epsilon_0^2 m^2 v_{\text{th}}^3} = \frac{ne^4}{16\pi\epsilon_0^2 m^{1/2} T^{3/2}}, \tag{2.5}$$

where the main takeaway is that the thermal collision frequency scales as $T^{-3/2*}$.

These scalings play an important role during a tokamak disruption. The electrical conductivity σ scales as $1/\nu_{\text{th}}$, which gives a temperature scaling according to $\sigma \sim T^{3/2}$, so that a drop in temperature is accompanied by a drop in the conductivity. The conductivity after the temperature drop has a major impact on the dissipation rate of the current, and thus on the electromagnetic forces exerted on the machine. In addition, as the current in an inductive system can not change instantly, a fast drop in the conductivity has to be compensated by a large induced electric field[†].

Consider now a superthermal electron (with $v \gg v_{\text{th}}$) moving through the plasma in the presence of such an induced electric field. The relative velocity compared to particles in the thermal bulk is then dominated by the velocity v, and the drag force therefore scales as $F_{\text{drag}} \sim mv\nu \propto 1/v^2$. Thus, for electrons with a velocity higher than a critical speed at which the acceleration force due to the electric field exceeds the drag force, the electric field can quickly accelerate the light electrons in the plasma to extremely high energies, forming a beam of runaway electrons, as will be discussed in more detail later in section 2.2.2. Before turning to the details of the runaway electron phenomenon, we give an overview of the kinetic equation, and in particular the so-called Coulomb collision operator, needed to rigorously model Coulomb collisions in a kinetic framework.

*We adopt the convention in plasma physics to include the Boltzmann factor k_B in the temperature, so that T has the dimension of energy.

†This is quite similar to the high voltages that may occur when one disconnects the power supply from an ordinary coil, as the reader might be familiar with from circuit theory.

2.2 The kinetic equation

In a kinetic model, a particle species in a plasma is described by the distribution of this species in position and velocity space, $f(\mathbf{r}, \mathbf{v}, t)$ (Chen, 1974). As $\mathbf{r}$ and $\mathbf{v}$ both represent three variables each, the distribution function is a function of seven variables. It is customary to normalize the distribution function so that its integral over the velocity space gives the particle density,

$$n(\mathbf{r}, t) = \int f(\mathbf{r}, \mathbf{v}, t) d\mathbf{v}. \tag{2.6}$$

The evolution of the distribution function is governed by the equation referred to as the *Boltzmann equation* or *kinetic equation*, which has the form (Chen, 1974)

$$\frac{\partial f}{\partial t} + \mathbf{v} \cdot \nabla f + \frac{\mathbf{F}}{m} \cdot \frac{\partial f}{\partial \mathbf{v}} = \left(\frac{\partial f}{\partial t} \right)_{\mathrm{c}} + S. \tag{2.7}$$

Here, ∇ is the gradient in position space, $\partial/\partial\mathbf{v}$ is the gradient in velocity space, and $\mathbf{F}$ is the force acting on the particles, usually the electromagnetic force $\mathbf{F} = q(\mathbf{E} + \mathbf{v} \times \mathbf{B})$. The right hand side contains the effect on the distribution function caused by collisions via the so-called *collision operator* $\left(\frac{\partial f}{\partial t}\right)_{\mathrm{c}}$. The source term S represents changes in the total number of particles, for example caused by ionization or recombination (where a free electron is caught by an ion). The left hand side may be recognized as the total time derivative df/dt of the distribution function, i.e. the time derivative in a frame of reference following the particles in the six-dimensional phase space, by invoking the chain rule, and recognizing that $d\mathbf{v}/dt = \mathbf{F}/m$ from Newton's second law. The kinetic equation can therefore be regarded as a mathematical formulation of the following rather intuitive statement: the distribution function in the frame advected along collisionless particle trajectories in phase space can only change due to collisions and sources.

2.2.1 The Fokker-Planck Coulomb collision operator

When deriving an expression for the collision operator for Coulomb collisions, the fact that the dynamics is dominated by small angle collisions makes it possible to describe the dynamics using a *Fokker-Planck collision operator*, which has the form (Rosenbluth, MacDonald & Judd, 1957; Helander & Sigmar, 2005)

$$\left(\frac{\partial f}{\partial t} \right)_{\mathrm{c}} = C(f) = \sum_k \sum_l \frac{\partial}{\partial v_k} \left[-\frac{\langle \Delta v_k \rangle}{\Delta t} f + \frac{\partial}{\partial v_l} \left(\frac{\langle \Delta v_k \Delta v_l \rangle}{2\Delta t} f \right) \right]. \tag{2.8}$$

The first term can be interpreted as a friction force, a form of advection in velocity space, and the second term describes a diffusion process in velocity space. The expression $\langle \Delta v_k \rangle$ should be understood as the expectation value of the velocity change along direction $k \in (x, y, z)$ during a short time Δt along a particle trajectory, due to the collisional contribution from all other particles. These expectation values can be evaluated based on a calculation of the velocity change in the single particle collision depicted in the right panel of figure 2.1, assuming small deflection angles.

Next, the number of collisions with a given velocity and impact parameter of the incident particles is calculated, in terms of the distribution function of the incident species. Once these quantities are known, the expectation value for the total velocity change can be obtained by integrating their product over velocity space and impact parameters.

If there are multiple species $b_1, b_2, ..., b_n$ colliding with species a, the total collision operator for species a is given by the sum

$$C_a(f_a) = \sum_{k=1}^{n} C_{ab_k}(f_a, f_{b_k}). \tag{2.9}$$

The notation C_{ab_k} should be interpreted as the collision operator for collisions of species a against species b_k, and f_a, f_{b_k} are the distribution functions for species a and b_k, respectively.

In many cases, deriving the terms on the right-hand side of equation (2.8) can be simplified by certain assumptions for the distribution function of the background species. One such case is collisions between particles of disparate speeds, e.g. collisions between electrons (denoted e) and ions (denoted i) with similar temperatures. The large mass ratio implies the ions move much slower, and the distribution function f_i can therefore be approximated by a delta function around $v' = 0$. The resulting collision operator for electron-ion collisions takes the form (Helander & Sigmar, 2005)

$$C_{ei} = \nu_{ei}(v)\mathcal{L}(f_e), \tag{2.10}$$

where the electron-ion collision frequency is $\nu_{ei}(v) = n_i Z_{\text{eff}} e^4/(4\pi m_e^2 \epsilon_0^2 v^3)$, $\mathcal{L}(f_e)$ is the Lorentz operator, and the *effective ion charge* Z_{eff} (given in terms of the elementary charge) is defined as (Helander & Sigmar, 2005)

$$Z_{\text{eff}} \equiv \frac{\sum_k \sum_l n_{b_k l} Z_{b_k l}^2}{\sum_i \sum_j n_{b_k l} Z_{b_k l}}, \tag{2.11}$$

where $n_{b_k l}$ and $Z_{b_k l}$ are the density and charge number respectively of charge state l of ion species b_k. The collision operator (2.10) is proportional to the angular part of the Laplacian operator in velocity space, meaning that C_{ei} describes a diffusion process on a sphere in velocity space at constant speed. As a result, only the direction of the electrons are changed by collisions with the massive ions.

The above approximation based on the disparate speeds of the colliding particles is not valid for electron-electron collisions. However, in many cases, such as the ones considered in this thesis, the electron distribution is dominated by a bulk population in thermal equilibrium, which can be used to simplify the collision operator. In a collisionally dominated, relativistic plasma, the equilibrium state is the Maxwell-Jüttner distribution (referred to as a Maxwellian for short). Thus, we divide the electron distribution function into a Maxwellian part, f_{e0}, and a non-Maxwellian part, $f_{e1} = f_e - f_{e0}$, containing far fewer particles than f_{e0}.

The collision operator can be shown to be bilinear (Helander & Sigmar, 2005), so that the collision operator can be expanded as

$$C_{ee}(f_{e0} + f_{e1}, f_{e0} + f_{e1}) = C_{ee}(f_{e0}, f_{e0}) + C_{ee}(f_{e0}, f_{e1}) + C_{ee}(f_{e1}, f_{e0}) + C_{ee}(f_{e1}, f_{e1}). \tag{2.12}$$

The first term vanishes, as the collision operator for collisions between two Maxwellians with the same temperature and average velocity is zero (Helander & Sigmar, 2005). If f_{e1} is small compared to f_{e0}, the last, nonlinear, term can also be neglected. The two remaining terms now comprise a *linearised electron-electron collision operator*. The first of these, called the *field particle term*, describes the effect on the Maxwellian bulk from collisions with the small non-Maxwellian population. The second, called the *test particle term*, describes the effect on the non-Maxwellian population from collisions with the Maxwellian.

If one is primarily interested in the evolution of the small non-Maxwellian part, it is usually sufficient to only keep the test particle term $C_{ee}(f_{e1}, f_{e0})$. Combined with the impact from electron-ion collisions, the collision operator describing the dynamics of the non-Maxwellian population then takes the form (Helander & Sigmar, 2005)

$$\begin{aligned} C_{e1}(f_{e1}) &= C_{ei}(f_{e1}) + C_{ee}(f_{e1}, f_{e0}) \\ &= \nu_{ei}\mathcal{L}(f_{e1}) + \nu_{\mathrm{D}}^{ee}\mathcal{L}(f_{e1}) + \frac{1}{v^2}\frac{\partial}{\partial v}\left[v^3\left(\frac{1}{2}\nu_{\mathrm{s}}^{ee}f_{e1} + \frac{1}{2}\nu_{||}^{ee}v\frac{\partial f_{e1}}{\partial v}\right)\right]. \end{aligned} \tag{2.13}$$

Here, the terms describe angular scattering, frictional drag, and a parallel velocity space diffusion, respectively. The collision frequencies ν_{ei}, ν_{D}^{ee}, ν_{s}^{ee} and $\nu_{||}^{ee}$ relevant in a tokamak disruption in general contain contributions from both free and bound electrons, as the temperature becomes low enough that the plasma partially recombines, and the frequencies are thus complicated by the quantum mechanical properties of the partially ionized ions and atoms (Hesslow *et al.*, 2018*a*). However, for a non-relativistic, fully ionized plasma, they reduce to the relatively simple expressions

$$\nu_D^{ee} = \hat{\nu}_{ee}\frac{\mathrm{erf}(x) - G(x)}{x^3}, \tag{2.14}$$

$$\nu_S^{ee} = 4\hat{\nu}_{ee}\frac{G(x)}{x}, \tag{2.15}$$

$$\nu_{||}^{ee} = 2\hat{\nu}_{ee}\frac{G(x)}{x^3}, \tag{2.16}$$

$$\hat{\nu}_{ee} = \frac{n_e e^4 \ln\Lambda}{4\pi\epsilon_0^2 m_e^2 v_{\mathrm{th}}^3}. \tag{2.17}$$

The dimensionless factor $\ln\Lambda$ is the so-called *Coulomb logarithm*, typically of order 10^1, and provides a measure of the impact of small angle collisions compared to large angle collisions (Chen, 1974).

We may note here that the average friction force on a particle, $-m_e v\nu_S^{ee}$, is proportional to the so-called Chandrasekhar function,

$$G(x) = \frac{\mathrm{erf}(x) - x\mathrm{erf}'(x)}{2x^2}, \tag{2.18}$$

where erf is the error function and the normalized speed $x = v/v_{\mathrm{th}}$ (Helander & Sigmar, 2005). This function decreases as $1/x^2$ for large x, in line with what we found for F_{drag} in the qualitative analysis of section 2.1. This fact gives rise to the runaway phenomenon, to which we now turn our attention.

2.2.2 The runaway phenomenon

The runaway phenomenon can be understood by studying the velocity dependence of the drag force felt by an electron moving through the plasma, the form of which is illustrated in figure 2.2. This non-monotonic velocity dependence means that, in the presence of an accelerating electric field E, once a particle has gained a speed higher than a critical speed marked as v_c in figure 2.2, the drag force will never balance the accelerating force. The particle can then continue accelerating to extremely high energies. This phenomenon is called the *runaway phenomenon*, and electrons with a speed larger than v_c are called *runaway electrons* (Helander & Sigmar, 2005). For such electrons, the energy gain is only limited by the energy losses due to synchrotron radiation and bremsstrahlung, which become significant at very high energies (Hirvijoki *et al.*, 2015; Embréus, Stahl & Fülöp, 2016).

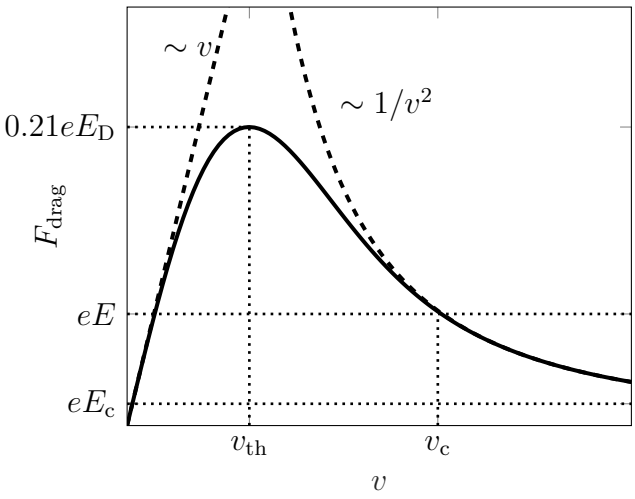

Figure 2.2: Illustration of the drag force felt by an electron moving through a plasma as a function of velocity. The presence of an accelerating electric field E creates a runaway region at velocities larger than v_c, where the drag force becomes weaker than the accelerating electric force. The Dreicer field E_D and the critical electric field E_c are also marked.

If the electric field becomes large enough, the accelerating force will be stronger than the maximum friction force. When this happens, all electrons become runaways. An estimate of the electric field required for this to happen can be obtained by inserting $v = v_\mathrm{th}$ in the asymptotic expression for the drag force at high velocities. The electric field E_D corresponding to this force is called the *Dreicer electric field* and is given by

$$E_\mathrm{D} = \frac{e^3 n \ln\Lambda}{4\pi\epsilon_0^2 T}. \tag{2.19}$$

When considering the full expression for the drag force, it can be shown that the electric field at which all electrons become runaways is approximately equal to $0.21E_\mathrm{D}$ (Helander & Sigmar, 2005).

As the electron speed is limited by the speed of light, one may anticipate from the classical treatment that the drag force does not go all the way down to zero at high velocities. This sets a lower limit on the electric field necessary for the existence of runaway electrons. A relativistic treatment in the high energy limit shows that,

in a fully ionized plasma, the drag force approaches the force corresponding to the Connor-Hastie critical electric field (Helander & Sigmar, 2005),

$$E_{\mathrm{c}} = \frac{e^3 n \ln\Lambda}{4\pi\epsilon_0^2 mc^2}. \tag{2.20}$$

During normal tokamak operation, due to the very high conductivity, an electric field of the order of 1 mV/m is sufficient to drive the plasma current, which is usually not high enough to enable runaway generation. The situation might however be different in the case of a disruption, where the plasma suddenly cools (Hender *et al.*, 2007). Typically, the temperature drops in the thermal quench by about three orders of magnitude, resulting in a decrease in the conductivity by a factor of the order of $10^{-4} - 10^{-5}$ (recall the $\sigma \sim T^{-3/2}$ scaling from section 2.1). On the short time scale of the temperature drop, the current density is essentially constant, so that $E \sim 1/\sigma$. The electric field thus increases by a factor of $10^4 - 10^5$, and can become much larger than E_{c}, so that runaways can be generated. However, in order for a runaway current to actually form, there must be some mechanism feeding electrons to the velocity space region above the critical velocity for runaway acceleration. Depending on the circumstances, a number of such mechanisms may be present in tokamak disruptions, as described below.

The runaway generation mechanisms can be divided into two different types: *primary generation* or *seed generation*, that is independent of the number of previously present runaway electrons, and *secondary generation* or *avalanche generation*, which amplifies an existing runaway seed. An example of the former is the *Dreicer mechanism* (Dreicer, 1959). This mechanism relies upon the fact that the velocity distribution tends to equilibrate collisionally towards a Maxwellian, with a high energy tail above the critical velocity. When this part of the distribution can run away, as particles accelerate to higher energies, the electron bulk will re-equilibrate and "fill out" the depleted tail, resulting in a continuous runaway generation.

The *hot-tail* mechanism of runaway generation occurs because it takes a finite time for the tail of the initially hot Maxwellian velocity distribution to equilibrate with the much lower temperature rapidly obtained by the bulk electrons during the thermal quench (Smith *et al.*, 2005; Smith & Verwichte, 2008). The equilibration of the tail of the distribution is slower than that of the bulk due to the velocity dependence of the collision frequency derived in section 2.1. The tail of the distribution might therefore temporarily form a non-Maxwellian electron population at superthermal energies. When the electric field increases at the start of the current quench, a part of this superthermal population may remain at velocities larger than the critical velocity, and in that way become runaways before they have time to thermalise. This mechanism is illustrated in figure 2.3, showing the evolution of the angle-integrated distribution function during a disruption, as simulated by the numerical tool DREAM described in chapter 4. As opposed to other mechanisms, the hot-tail generation is only present during the initial part of the disruption.

In non-nuclear experiments, using pure deuterium plasmas, the Dreicer and hot-tail mechanisms are the only primary runaway generation mechanisms. During nuclear operation, however, the power will be generated by fusing deuterium and tritium, with the latter being β^--radioactive. Part of the energy spectrum of the

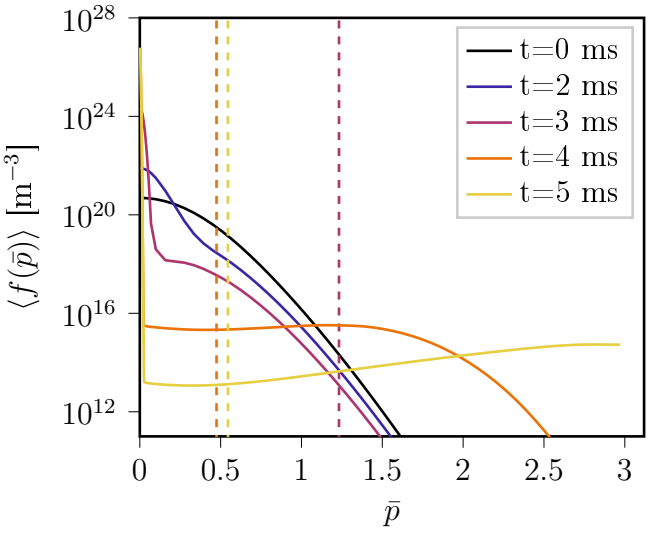

Figure 2.3: Illustration of the hot-tail mechanism, showing a representative evolution of the angle averaged electron momentum distribution $\langle f(\bar{p})\rangle$ as a function of the normalized momentum $\bar{p} = p/(m_e c)$. The vertical dashed lines indicate the runaway threshold momentum (initially outside the scale). The tail of the initially hot Maxwellian distribution (black line) takes a finite time to equilibrate to the dropping temperature of the bulk electrons. As the electric field increases, part of the distribution is therefore "caught" above the runaway threshold momentum, and is accelerated to higher momenta. The data is extracted from the disruption simulation studied in figure 5.6 a) in Vallhagen (2021).

electron released during the β^--decay may fall within the runaway region, providing another source of runaway generation (Martín-Solís, Loarte & Lehnen (2017), Paper **A**). Another runaway generation mechanism present during nuclear operation comes from the activation of the wall due to the bombardment by neutrons released in the fusion reactions. This bombardment makes the wall radioactive, causing it to emit γ-photons. These γ-photons can be Compton scattered against electrons in the plasma, transferring enough energy to an electron to accelerate it over the runaway threshold (Martín-Solís, Loarte & Lehnen, 2017).

Finally, the runaway generation by the above mechanisms may be amplified by the *avalanche mechanism*. This mechanism generates runaways through collisions of existing runaways with slower electrons in such a way that both electrons have final velocities larger than the critical one after the collision (Sokolov, 1979; Rosenbluth & Putvinski, 1997; Embréus, Stahl & Fülöp, 2018). As the energies of the runaway electrons are much higher than the ionization energy of the ions in the plasma, bound electrons may also contribute to the avalanche process. In fact, it has recently been shown that an increase in the fraction of bound electrons might substantially enhance the avalanche. The reason for this is that the bound electrons contribute to the number of target electrons to practically the same extent as the free electrons, while their contribution to the drag force is smaller than that from free electrons at high electric fields (Paper **E**).

Chapter 3

Disruption mitigation by massive material injection

We now move on to the main methods considered in order to achieve the disruption mitigation requirements mentioned in chapter 1. This is a very active field of research, to which this work aims to contribute. The strategies studied most extensively to date are based on various forms of material injection, and so-called shattered pellet injection has been chosen as the basis for the disruption mitigation system in ITER Lehnen *et al.* (2020); ITER organization. This chapter gives an overview of material injection in the context of disruption mitigation, leading up to the most advanced injection scheme suggested, the two-stage shattered pellet injection scheme, that is the focus of paper **C**.

Massive material injection act to mitigate disruptions in three main ways, corresponding to the requirements on the radiated fraction of the thermal energy, current quench time and runaway avoidance. Suitable materials for radiative dissipation of the thermal energy are noble gases such as neon or argon Hollmann *et al.* (2015). Also note that as long as some amount of the impurity is present, the radiation can be further enhanced by increasing the electron density by injecting e.g. hydrogen species, since the collisional excitation rate is proportional to the electron density. The quantity and composition of injected material can also be used to regulate the post-disruption temperature, which is roughly given by an equilibrium between the impurity radiation and the Ohmic heating. Since the current quench time is proportional to the conductivity, which in turn scales as $T^{3/2}$, the temperature essentially determines the current quench time.

Finally, the injected material might reduce the runaway generation due to the resulting electron density increase, leading to an increase in the critical electric field according to equation (2.20). It should however be noted that the usefulness of this method to reduce the runaway generation might be limited by the fact that if the injected quantity becomes too high, the cooling might be intense enough to cause a substantial recombination, which can severely increase the runaway avalanche, as mentioned in section 2.2.2 and discussed more thoroughly in paper **B**.

With the above general background about the purpose of massive material injection in mind, we now turn to the different injection schemes and methods proposed to deliver the injected material in the following sections.

3.1 Injection schemes

A particular difficulty for the disruption mitigation system is that the various requirements of the disruption mitigation are to some extent contradictory Hollmann *et al.* (2015). For the mitigation of the thermal loads, it would be beneficial to have an early large injection of strongly radiating material, such as argon or neon. Such injections could also substantially increase the electron density, which would contribute to the reduction of the runaway generation. Large amounts of argon or neon might however result in a post-thermal quench temperature too low to give an acceptable current quench time. Moreover, they might also increase the runaway seed generation from the hot-tail mechanism, as well as enhance the subsequent runaway avalanche due to the presence of bound electrons.

The currently envisaged compromise is to inject large amounts of deuterium combined with a trace amount of argon or neon Breizman *et al.* (2019); Lehnen *et al.* (2020). The role of the deuterium would be to provide a source of electrons in order to limit the runaway generation and to enhance the radiation efficiency of the neon. The role of the neon would be to radiatively dissipate the thermal energy and to set a post-thermal quench equilibrium temperature within an acceptable range.

A recently suggested improvement to the above scheme is to divide the injection into two stages following rapidly after each other Nardon *et al.* (2020*b*). The first stage would then deliver the deuterium, and the second deliver the neon or argon. The aim of such a scheme would be to first cool the plasma by dilution down to the 100-1000 eV range by the pure deuterium injection, without perturbing the plasma pressure or current density enough to significantly accelerate the growth of MHD instabilities (introduced in section 1.2). The plasma would then be left at this temperature for a few milliseconds to let the full distribution equilibrate to a Maxwellian at this temperature. A final radiative thermal quench would then be triggered by injecting the argon or neon. The intermediate equilibration of the distribution is expected to produce a significant reduction of the hot-tail runaway generation. The radiated fraction of the thermal energy could also be significantly increased, as the magnetic perturbations would not become significant until the comparatively low temperature makes conducted losses subdominant to radiation losses. It was indicated in by Nardon *et al.* (2020*b*) that it is possible to cool an ITER-like plasma by dilution down to ~ 100 eV without immediately triggering a major MHD instability. The runaway dynamics and radiation characteristics of such a two-stage SPI scheme is the subject of paper **C**.

For such a mitigation scheme to be successful, it is important to assimilate a large amount of deuterium over as much of the plasma volume as possible before the onset of the MHD instability. This poses strict requirements on the injection system, the design of which is discussed in the next section.

3.2 Injection techniques

The most straightforward injection method is *massive gas injection*, where the injected material is simply released into the tokamak in gaseous form, via a connector to a pressurized vault Hollmann *et al.* (2015). As the simplest proposed method

to implement, it is the one most studied experimentally, and therefore also theoretically. The greatest advantage with this method is its simplicity, while the assimilation efficiency of the released gas is found to be rather poor in practice on larger machines, despite promising results on smaller machines Papp *et al.* (2016); Reux *et al.* (2015). Much of the material has been observed in both experiments and simulations to be stopped at the plasma edge and only slowly mix with the rest of the plasma. This can be understood as a result of the fact that as soon as the gas particles ionize, they become confined by the magnetic field, which, together with the pressure of the pre-existing plasma, restricts the gas penetration. The resulting strong cooling at the edge may induce substantial MHD activity, which may help to speed up the inward transport of injected ions but also lead to an unwanted increase in the conducted heat losses.

Another method that gives a faster, more efficient delivery of material to the plasma core, is to inject the material in the form of solid cryogenic pellets Hollmann *et al.* (2015). In this way, the material travels through the plasma in a neutral, solid form, while being continuously ablated by the hot background plasma, depositing material along the trajectory. The pellets are typically accelerated by a propellant gas and reach speeds of around 300-600 m/s. This is similar to many typical gas sound speeds, and therefore the arrival time of the pellets at the plasma is not significantly different compared to a gas injection from the same location. Note that injection of pellets (though typically slightly smaller and of hydrogen isotopes) is regularly performed on existing machines, including for purposes other than disruption mitigation, such as to fuel the plasma, regulate instabilities and for diagnostic purposes Pégourié & Picchiottino (1996); Milora *et al.* (1995).

There are, however, a number of disadvantages associated with disruption mitigation by pellet injection. Depending on the speed at which the pellet travels and the state of the plasma, the pellet may pass through the plasma without depositing all of its material. Besides making the injection less effective, the remaining pellet might damage the wall upon impact (Hollmann *et al.*, 2015). This problem is particularly relevant when a pellet is injected after the plasma has already been cooled in the course of the thermal quench. One way to address this issue is to use an SPI (Baylor *et al.*, 2009; Breizman *et al.*, 2019). In an SPI, the pellet is shattered against a tilted plate before entering the plasma. The number of shards into which the pellet is shattered may be controlled (to some extent) by varying the speed and impact angle on the shattering plate. Increasing the number of shards (for a fixed total amount of pellet material) increases the ablation rate, hence reducing the amount of material passing through the plasma without ablating. The increased ablation may be understood by the fact that shattering the pellet increases the total contact area with the plasma. Any leftover material striking the wall will also be spread over a larger area, reducing the risk of damaging the wall. The initial spread of the deposited material is also increased, lowering the risk of local peaking in the radiative heat loads before the material has homogenized through the plasma.

Due to these advantages, SPI has been chosen as the basis of the ITER disruption mitigation system Lehnen *et al.* (2020); ITER organization. However, the design and operation parameters of the ITER disruption mitigation system, such as the pellet composition, the number of pellets and their particle contents, the degree of

shattering, timing aspects etc. remain open questions. In order to address these questions, it is important to be able to model the behavior of the pellet and its interaction with the background plasma. This is the subject of the next two sections concluding this chapter.

3.3 Pellet shattering and ablation

An SPI starts with a pellet being accelerated and then shattered against a tilted plate, resulting in a plume of pellet shards of different sizes and velocities entering the plasma. While in reality the distribution of pellet shard sizes has a more complicated dependence on the injection parameters such as the pellet size, velocity and shattering angle (Peherstorfer *et al.*, 2022), one may estimate the shard size distribution by considering the fact that the pellet is initially mostly broken by shear stresses into a saucer-like structure (Parks, 2016). If the further break-up of the thin layers thus formed is approximated as a division by a large number of randomly and independently distributed perpendicular straight lines, the probability density $P(r_\mathrm{p})$ of the shard radius (or, rather, shard length scale) r_p takes the form (Mott & Linfoot, 2006)

$$P(r_{p,k}) = k_p^2 r_{p,k} K_0(k_p r_{p,k}), \qquad k_\mathrm{p} = \left(\frac{N_\mathrm{inj}}{6\pi^2 n_\mathrm{p} N_\mathrm{s}}\right)^{-1/3}, \tag{3.1}$$

where K_0 is the zeroth modified Bessel function of the second kind, the pellet is assumed to be shattered into N_s shards, n_p is the number density of the solid pellet material, and N_inj is the total number of injected atoms. The parameter k_p can be interpreted as the inverse of the characteristic shard size. This distribution has a rather long tail towards large r_p, so that even if the pellet is shattered into many shards, a few larger shards, which may propagate deeper into the plasma before they are completely ablated, are typically present. Such a distribution of shard sizes has recently been used in several SPI modeling activities (Hu *et al.*, 2018; Matsuyama *et al.*, 2020; Nardon, Matsuyama & Lehnen, 2020), with N_inj and N_s being considered adjustable parameters.

Once the shards enter the plasma, they are continuously ablated, depositing their content along their trajectories. In essence, the number of particles ablated from a pellet or pellet shard during a given time interval is determined by the ratio of the heat flux reaching the pellet surface during this time interval and the sublimation energy per particle. However, on a very short timescale after the pellet is exposed to the plasma (of only a few μs), the finite flow of ablated material away from the pellet produces a dense cloud around the pellet that shields it from the heat flux from the plasma Pégourié (2007). The pellet ablation can therefore be regarded as a self-regulating process, balancing the heat flux coming from the plasma and the resulting build-up of the shielding cloud. The resulting quasi-stationary cloud size and ablation rate are such that only the ablation energy necessary for maintaining the cloud size reaches the pellet surface.

Directly above the pellet surface, the cloud is neutral and close to spherically symmetric. This neutral cloud typically has a thickness of the order of 1 cm, and a

particle density of $10^{25} - 10^{26}$ m^{-3}. The pellet (or pellet shard) itself typically has a thickness of the order of a millimeter. At the edge of the neutral cloud, the material density falls and the temperature increases enough to begin to ionize the ablated material. The material takes the form of a confined cold plasma, whose subsequent expansion is therefore mostly aligned with the field lines.

There are three main mechanisms involved in the shielding of the pellet by the neutral cloud, although usually of quite different importance Pégourié (2007). With decreasing importance, these mechanisms are referred to as *gas dynamic shielding*, *electrostatic shielding* and *diamagnetic shielding*. The gas dynamic shielding refers to the deposition of incident plasma energy by the collisional interaction with the neutral gas in closest proximity to the pellet. Collisions between the hot incident electrons and the new cold ablated plasma beyond the neutral cloud also contribute to some extent, but give a typically much smaller contribution (Parks & Turnbull, 1978; Pegourie *et al.*, 2002). The energy deposition in the cloud occurs due to scattering, heat transfer to the cloud particles, and ionization and excitation of ions and atoms in the cloud, which then dissipate the energy by radiation (Pégourié, 2007; Lengyel *et al.*, 1999). It has however been estimated that, due to its relatively high density, the cloud might be substantially opaque to the resonant lines. A significant fraction of the radiation might therefore be trapped within the cloud, and the corresponding energy also contribute to the cloud heating (Morozov *et al.*, 2004; MacAulay, 1994).

Electrostatic shielding results from the different mobility of ions and electrons (Pégourié, 2007). Electrons in the background plasma initially flow into the ablation cloud much faster than the ions, due to their lower mass. This gives rise to a difference in charge between the ablation cloud and the surrounding plasma, and the corresponding electrostatic potential difference limits the heat flux into the ablation cloud.

Diamagnetic shielding occurs as there is a finite timescale for the magnetic field to diffuse into the cloud (Pégourié, 2007). The gyration of the ionized particles in the ablation cloud creates a magnetic field that opposes the background magnetic field, hence the name diamagnetic shielding. The heat flux from the background plasma is guided by the magnetic field lines, so deflection of the magnetic field leads to a deflection of the heat flux around the ablation cloud. The importance of this effect can be characterized by the ratio of the flow speed of material away from the pellet and the speed of the diffusion of the magnetic field into the neutral cloud, which is not expected to be very large due to the comparatively low conductivity of the neutral cloud (Parks & Turnbull, 1978).

In reality, some further complications arise in addition to the picture described above. One such complication is that as the pellet moves through the plasma, it can periodically cross the boundary of the ablation cloud surrounding it and establish a new one upon direct exposure to the background plasma (Milora *et al.*, 1995). This periodicity might explain the striations in the deposition profile sometimes observed in experiments. Another complication is that the ablation is not completely symmetric around the pellet (Pégourié, 2007; Milora *et al.*, 1995). Reasons for this include the difference in the heat flux parallel and anti-parallel to the electric field driving the plasma current. This makes the ablation cloud thicker in the direction

anti-parallel to the electric field. Another source of cloud asymmetry is irregularities in the pellet shape. Asymmetric ablation might give rise to a "rocket-like" effect, propelling the pellet in the opposite direction to the increased ablation. In many theoretical models, however, these subtleties are not accounted for.

As the gas dynamic shielding is typically the dominating shielding mechanism, most models of pellet ablation are centered around a treatment of this mechanism, possibly including corrections for other shielding mechanisms. This allows for several simplifications of the problem, leading to the so-called *Neutral Gas Shielding (NGS) model* described in the next subsection.

3.3.1 The Neutral Gas Shielding model

As the gas dynamic shielding mostly takes place close to the pellet surface, where the shielding cloud is essentially spherically symmetric, it is a reasonable approximation to reduce the problem to one, radial, dimension (although the incoming particle and heat flux is significantly higher along than across the magnetic field lines). Moreover, as the time scale for the build-up of the shielding cloud is in the μs-range, which is about 2-3 orders of magnitude faster than most other processes of interest, the problem may be treated as quasi-stationary. The ablation rate can then be found by self-consistently solving the spherically symmetric conservation equations for mass, momentum and energy, together with the ideal gas equation of state, with a boundary condition at the pellet surface determined by the gas-solid phase transition there. The energy is primarily deposited in the cloud by the light electrons of the bulk plasma, which stream rapidly along the field lines to intersect the pellet. For pellets containing a large fraction of hydrogen isotopes that have a sublimation energy per particle of only a fraction of an electron volt, the boundary condition can be expressed by requiring the heat and particle flux to completely vanish at the pellet surface. The solution to the equation system thus obtained yields the NGS model (Parks & Turnbull, 1978).

Several analytical solutions for the pellet ablation rate within the above setup have been determined in the literature, using different models for the energy attenuation inside the cloud and including different corrections for additional mechanisms limiting the ablation. However, the mass ablation rate G (in kg/s) can typically be expressed as a scaling law in terms of the incoming heat flux q_{in}, the effective energy $\mathcal{E}_{\mathrm{in}} = 2T$ of the incoming electrons, and the pellet radius r_{p}, according to (Parks & Turnbull, 1978; Fontanilla & Breizman, 2019)

$$G = -\lambda \left(\frac{q_{\mathrm{in}}}{q_0}\right)^{1/3} \left(\frac{\mathcal{E}_{\mathrm{in}}}{\mathcal{E}_0}\right)^{7/6} \left(\frac{r_{p,k}}{r_{p0}}\right)^{4/3}. \tag{3.2}$$

Here, q_0, $\mathcal{E}_0$ and r_0 are characteristic values of the incoming heat flux, effective energy and pellet radius, respectively, and the details of the energy attenuation model enter via the pre-factor λ *.

The original treatment was done by Parks & Turnbull (1978) for pure hydrogen pellets. The energy distribution of the incident electrons from the bulk plasma

*The exponents are also slightly dependent on the energy attenuation model, but usually to a negligible extent (Fontanilla & Breizman, 2019; Parks, 2017; Parks & Turnbull, 1978).

was approximated by a single mono-energetic beam with effective energy per particle $\mathcal{E}_{\text{in}} = 2T$, equal to the ratio of the unidirectional heat and particle flux, and the model for the electron energy absorption and scattering consisted of empirical expressions specific for hydrogen isotopes.

This model has later been improved upon, and adapted to various situations, e.g. by treating the full Maxwellian energy distribution of the incident particles instead of a mono-energetic beam (MacAulay, 1994; Fontanilla & Breizman, 2019), by treating pellets consisting of higher atomic number material (Parks, Leffler & Fisher, 1988; Fontanilla & Breizman, 2019), or including the shielding due to the still cold plasma expanding along the field lines outside the neutral cloud (Pegourie *et al.*, 2002). The ITER disruption mitigation system will use pellets consisting of a mixture of neon and hydrogen isotopes, creating a particular interest for an NGS model adapted to such pellets. The most up to date version of the NGS model adapted to this situation, accounting for the full Maxwellian electron momentum distribution was presented by Parks (2017). With the normalising radius, heat flux and effective energy given by $r_{p0} = 2$ mm, $q_0 = n_0\sqrt{2T_0^3/(\pi m_e)}$ and $\mathcal{E}_0 = 2T_0$, with the representative temperature and density $T_0 = 2000$ eV and $n_0 = 10^{20}$ m^{-3}, respectively, the pre-factor λ becomes

$$\lambda(X) = [27.0837 + \tan(1.48709X)]/1000 \text{ kg/s}, \tag{3.3}$$

where $X = N_{\text{D}_2}/(N_{\text{D}_2} + N_{\text{Ne}})$ is the deuterium fraction, N_{D_2} is the number of deuterium molecules and N_{Ne} is the number of neon atoms in the pellet. This model has been used in many recent studies of disruption mitigation by SPI in ITER (Nardon *et al.*, 2020*b*; Hu *et al.*, 2018; Matsuyama *et al.*, 2020), including paper **C**.

3.4 Deposition of the ablated material

Once the pellet material is ablated and ionized, it begins to homogenize over the flux surfaces, and the pressure and temperature start to equilibrate with the background plasma. In present day machines, the homogenization process takes place over a time scale of 0.1-1 ms Pégourié & Picchiottino (1996). There are two main processes responsible for the homogenization. The first is the excess pressure of the cold plasmoid of ablated material driving its expansion along the magnetic field, at a speed similar to the sound speed inside the plasmoid. As a field line covers a whole flux surface[†], the expansion along the field lines eventually leads to the material being homogenized over the entire flux surface. This mechanism alone has however been shown to give about an order of magnitude slower equilibration than the 0.1-1 ms time scale observed in experiments Pégourié & Picchiottino (1996).

An additional mechanism to consider in describing the homogenization is caused by the potential difference between the channel of ablated material and the background plasma, again arising due to the much larger mobility of electrons compared

[†]This is technically not true for the countable number of rational flux surfaces where the number of poloidal to toroidal turns of the field line is a ratio of integers. However, due to the finite gyroradius and the cross-field drift described below in section 3.4.1, the particles are not strictly confined to a single flux surface, which effectively reduces the effect of the rational flux surfaces.

to ions. As the channel of ablated material is heated while still having a much larger density than the background plasma, the net flow of negative charge will go from the channel of ablated material into the background plasma. The gradient along the tokamak minor radius of this potential gives rise to an electric field along the minor radius, which in turn causes an $E \times B$-drift in the poloidal direction. Conservation of momentum on the flux surface where the channel of ablated material resides then gives rise to a poloidal rotation of the plasma in the direction opposite to the poloidal $E \times B$-drift of the ablated material. The gradient of this rotation along the minor radius, together with the variation of the background magnetic field direction, gives rise to a poloidal stretching of the ablated material. As the ablated material is thinned out, the collisional interaction with the background plasma and the small scale turbulence becomes more effective, and eventually the ablated material equilibrates with the background plasma. The above mechanisms together have been shown to give rather accurate reproductions of the time evolution of the background plasma following fueling pellet injections in experiments Pégourié & Picchiottino (1996).

Finally, yet another $E \times B$-related drift might be present that transports the ablated material across the flux surfaces Parks & Baylor (2005). The limited length along the toroidal field line of the initial expanding channel of ionised, ablated material, re-introduces the issue of vertical charge separation in the channel by the ∇B drift. Remember this issue was described in chapter 1, occurring in the whole tokamak in the absence of a poloidal magnetic field. This gives rise to a vertical electric field in the vicinity of the ablated material, causing an $E \times B$ drift of the ablated material along the major radius towards the low magnetic field side. This cross-field drift results in a shift of the final deposition profile compared to the deposition profile immediately following the ablation. There is a wealth of experimental observations of this effect in present-day tokamaks (Baylor *et al.*, 2007; Lang *et al.*, 1997), and numerical simulations indicate that it might have a substantial impact in ITER (Matsuyama, 2022). This phenomenon is also the subject of paper **D**, and is described further in the next subsection.

3.4.1 Cross-field drift

The size of the outward shift of ablated pellet material resulting from the cross-field drift is regulated by three main mechanisms, related to the decay of the excess pressure inside the plasmoid, the twisting of the magnetic field lines, and additional currents counter-acting the charge separation (Pégourié *et al.*, 2006; Rozhansky *et al.*, 2004; Parks, Sessions & Baylor, 2000). The excess current due to the ∇B drift inside the plasmoid compared to the background plasma is proportional to the excess pressure inside the plasmoid. Thus, as the plasmoid expands and the excess pressure decreases, so does the driving force behind the drift motion. Moreover, as the plasmoid expands around the torus along the twisted magnetic field lines, the vertical position of the field lines is inverted for the inboard portion of the plasmoid compared to the outboard portion, and when this happens the magnetic drift currents in the outboard and inboard portions of the plasmoid cancel out (analogously to a tokamak equilibrium). This mechanism effectively stops the drift

motion over a characteristic time scale given by the time it takes for the cloud to expand one connection length along the field lines, $t_{\rm drift} \sim \pi R_{\rm m} q/c_{\rm s}$, where $R_{\rm m}$ is the major radius, $c_{\rm s}$ is the sound speed inside the plasmoid and q is the safety factor. Finally, the electric field resulting from the charge separation gives rise to additional currents counter-acting the charge separation, which limit the build-up of the electric field and hence the $E \times B$ drift.

The radial component of the $E \times B$ drift, $v_{\rm d} = \mathbf{E} \times \mathbf{B}/B^2 \cdot \hat{R} \approx E_y/B$ (Chen, 1974), is proportional to the binormal (nearly vertical) electric field E_y inside the plasmoid (considering $t \ll t_{\rm drift}$, i.e. disregarding the twisting of the field lines, for simplicity, referring to paper **D** for a more detailed picture). Moreover, the vertical electric field, as well as the density and temperature, may be approximated as constant along the field lines inside the plasmoid Pégourié *et al.* (2006). The equation of motion of the cloud can thus be formulated as a condition for the current to be divergence free in the quasi-neutral plasma, as illustrated in figure 3.1.

For $t \ll t_{\rm drift}$, the total ∇B current per unit length in the radial direction is approximately given by (Rozhansky *et al.*, 2004)

$$J_{\nabla B} \approx -\frac{2\Delta p L_{\rm cld}}{B R_{\rm m}}, \tag{3.4}$$

where Δp is the excess pressure and $L_{\rm cld}$ is the length of the plasmoid. This current is balanced by the current driven by the electric field inside the cloud, counter-acting the charge separation, which is in turn comprised of three main components. The first one is driven by the time variation of the electric field. The time variation of the electric field causes an acceleration of the $E \times B$ drift, which the drifting particles experience as a force. In a similar way as the force from the electric field gives rise to the $E \times B$ drift, the force corresponding to the time variation of the electric field gives rise to an additional drift, called the *polarisation drift*. This drift is perpendicular to both the magnetic field and the $E \times B$ drift, and is therefore directed in the vertical direction in this case, as shown in figure 3.1. The corresponding current per unit length in the radial direction is given by Pégourié *et al.* (2006)

$$J_{\dot{E}} = \frac{\bar{\rho}}{B^2} \frac{dE_y}{dt}, \tag{3.5}$$

where $\bar{\rho}$ is the field line-integrated mass density inside the plasmoid.

The two remaining contributions come from currents exiting the plasmoid parallel to the field lines. One of these currents is carried by the Alfvén waves traveling along the field lines, excited by the gradient in the electrostatic potential imposed by the charge separation inside the plasmoid. Initially, before any of the Alfvén waves emitted from the opposite sides of the cloud have started to interfere with each other, this current contribution can be described by the Alfvén resistivity $R_{\rm A} = \mu_0 c_{\rm A}$, where μ_0 is the vacuum permeability and $c_{\rm A} = B/\sqrt{\mu_0 \rho} \gg c_{\rm s}$ is the Alfvén speed (Rozhansky *et al.*, 2004). The resulting parallel current per unit length in the radial direction becomes

$$J_{\rm A} = 2\frac{E_y}{R_{\rm A}}. \tag{3.6}$$

The factor 2 comes from the fact that the current flows from both sides of the plasmoid.

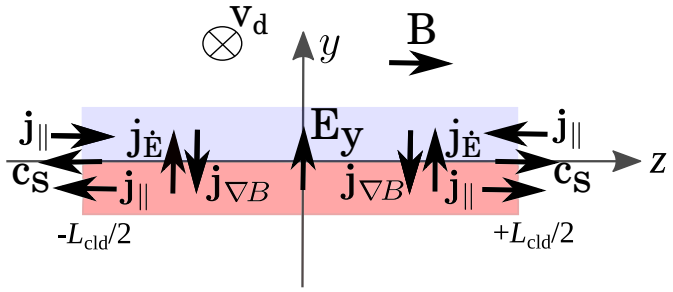

Figure 3.1: Toroidal cross section of a plasmoid of ablated pellet material, showing the contributions to the current balance determining the vertical electric field E_y and the corresponding drift velocity (in the radial direction). The positively (lower) and negatively (upper) charged parts of the plasmoid are marked with red and blue, respectively. The plasmoid expands in the z-direction, parallel to the magnetic field, at the speed of sound c_s, and the drift motion is directed into the paper.

When the Alfvén waves traveling along a set of field lines meet the Alfvén waves traveling from the opposite side of the plasmoid, these waves interfere so that the electrostatic potential starts to converge towards a quasi-steady, nearly linear, variation along these field lines. At this point, these field lines effectively form a coil along which the current can be described by Ohm's law. Every time the Alfvén waves travel one toroidal turn around the torus, a portion of the field lines (statistically) will "connect" in this way to the opposite side of the plasmoid, so that an increasing fraction of the field lines start to carry an ohmic current instead of an Alfvénic current. The total parallel current contribution thus takes the form (Pégourié *et al.*, 2006)

$$J_{||} = J_\mathrm{Ohm} + J_\mathrm{A} = \frac{E_y}{R_\mathrm{eff}} + 2P_\mathrm{A}\frac{E_y}{R_\mathrm{A}}, \tag{3.7}$$

where P_A is the fraction of the field lines still carrying an Alfvénic current, and R_eff is the effective resistance of the Ohmic current, determined by the background plasma conductivity and the length of every set of field lines connecting to the opposite side of the plasmoid.

The total current balance equation thus takes the form of a first-order ODE, according to

$$J_{\nabla B} + J_{\dot{E}} + J_\mathrm{A} + J_\mathrm{Ohm} = -\frac{2\Delta p L_\mathrm{cld}}{BR_\mathrm{m}} + \frac{\bar{\rho}}{B^2}\frac{dE_y}{dt} + \frac{E_y}{R_\mathrm{eff}} + 2P_\mathrm{A}\frac{E_y}{R_\mathrm{A}} = 0. \tag{3.8}$$

This model was originally studied by Pégourié *et al.* (2006) and Commaux *et al.* (2010) to examine the parameter dependence of the pellet drift and validate the model by comparing the resulting density build-up against experiments. They used a numerical model for the plasmoid density, temperature and size, as well as the effective resistance for the Ohmic current, and accounting for the poloidal twist of the field lines by limiting the integration time to t_drift. A more detailed derivation of the equation of motion for the plasmoid drift, along with an analytical solution, is presented in paper **D**, including an improved treatment of the poloidal twist of the magnetic field lines and an analytical model for R_eff.

Chapter 4

Disruption model

Having acquired a basic knowledge of the characteristic features of disruptions, and the proposed injection schemes to mitigate their impact, we are now in a position to describe the models used in this work to simulate such scenarios in papers **A**-**C**. A number of components are required to build a model for the injected material deposition through the final current decay, and they are described in the sections of this chapter. The model for the evolution of the electron and ion density, possibly including a source due to an ablating pellet, is described in section 4.1, and the model describing the subsequent plasma cooling is described in section 4.2. The cooling of the plasma is accompanied by a drop in the conductivity, leading to the induction of a strong electric field, after which the plasma current starts to decay. The strong electric field might however lead to the generation of a substantial runaway current, as was also described in section 1.2, resulting in an incomplete current decay. The evolution of the electric field, as well as the models governing the runaway generation resulting from the induced electric field, are described in section 4.3. Finally, the numerical tools GO (Fehér *et al.* (2011), Paper **B**), and DREAM (Hoppe, Embreus & Fülöp, 2021) are described in section 4.4. These codes solve the set of equations listed in this chapter starting from a set of given injection parameters and pre-disruption plasma parameters.

4.1 Material injection and density evolution

The density evolution is determined by summing the contributions from the ionization/recombination processes and the material injection. As mentioned in section 3.4, the homogenization of the ablated material over the flux surfaces, as well as the temperature and pressure equilibration with the background plasma, occurs over a time scale $\lesssim 1$ ms. This time scale is comparable to the thermal quench time scale, while being relatively fast compared to the current quench time scale. The homogenization and equilibration of the ablated material is therefore approximated here to take place instantaneously, an assumption also made in other recent disruption mitigation studies (Nardon *et al.*, 2020*b*; Matsuyama *et al.*, 2020; Nardon, Matsuyama & Lehnen, 2020; Shiraki *et al.*, 2020). Similarly, all other quantities involved, except for the pellet shard positions and radii in case of an SPI, are assumed to be constants over the flux surfaces. In this work, the flux surfaces are

assumed to have concentric elliptical cross-sections, with elongation $\kappa(r)$, and are labeled with their mid-plane minor radius r. Moreover, we employ the large aspect ratio limit $R_\mathrm{m}/a \gg 1$, where R_m and a are the major and minor radii of the plasma, respectively, so that the spatial geometry becomes elliptic-cylindrically symmetric*. The flux surface geometry is assumed to be constant in time.

With n_{ij} denoting the density of charge state i of ion species j, the change in the local charge state distribution of all ions due to ionization and recombination is calculated by the time dependent rate equations

$$\left(\frac{\partial n_{ij}}{\partial t}\right)_\mathrm{ioniz} = I_{i-1,j}n_{i-1,j}n_\mathrm{M} - I_{ij}n_{ij}n_\mathrm{M} + R_{i+1,j}n_{i+1,j}n_\mathrm{M} - R_{ij}n_{ij}n_\mathrm{M}, \tag{4.1}$$

where $I_{ij}(T_\mathrm{M}, n_\mathrm{M})$ and $R_{ij}(T_\mathrm{M}, n_\mathrm{M})$ are the ionization and recombination rates, with n_M and T_M denoting the density and temperature of the thermal, Maxwellian, electron bulk, respectively (recall the division of the electron distribution function discussed in section 2.2.1). In this work, these ionization/recombination rates are interpolated from tabulated values of numerical calculations of the excitation/deexcitation processes involved, available in the ADAS (Summers, 2004) and AMJUEL† databases. Thus, the total evolution of the charge state densities is given by

$$\frac{\partial n_{ij}}{\partial t} = \left(\frac{\partial n_{ij}}{\partial t}\right)_\mathrm{ioniz} + \left(\frac{\partial n_{ij}}{\partial t}\right)_\mathrm{injection}. \tag{4.2}$$

The corresponding evolution of the total free electron density n_free (including both the Maxwellian and non-Maxwellian populations) is determined by the condition that the plasma must remain quasi-neutral.

The injection can be modeled in a number of different ways depending on the injection technique, with varying degree of simplicity and sophistication. The simplest way to model an arbitrary type of injection is to assume the injected material to be instantly deposited in the neutral charge state at $t = 0$, with a prescribed spatial profile. This profile may be chosen to be rather homogeneous, motivated by the rapid flattening of the density profile due to the enhanced transport occurring when the magnetic field becomes stochastic. As the injection time scale is similar to the thermal quench time scale, and 1-2 orders of magnitude shorter than the current quench time scale, this model may be sufficient to capture the main characteristics of the disruption, especially the current evolution, and has therefore been used in several studies available in the literature (Izzo *et al.* (2011); Martín-Solís, Loarte & Lehnen (2017), Paper **B**).

This model is however not sufficient to capture the detailed evolution of all quantities of interest, and does not treat the question of how the injected material is assimilated. In case of a pellet injection or SPI, this would instead require resolving the ablation and propagation of the pellet or pellet shards. The homogenized ion density increase on the flux surface with radius r due to the ablation of the pellet material is then given by

$$\left(\frac{\partial n_{ij}}{\partial t}\right)_\mathrm{injection} = -f_{ij}\sum_{k=1}^{N_\mathrm{s}} \frac{4\pi r_{p,k}^2 \dot{r}_{p,k}\rho_\mathrm{dens}N_\mathrm{A}}{\mathcal{M}} H(r, \rho_{p,k}), \tag{4.3}$$

*Note, however, that a more advanced geometry is now available in the DREAM code.
†http://www.eirene.de

where the time derivative $\dot{r}_{p,k}$ of the k^{th} shard is related to the mass ablation rate G_k of the same shard according to $\dot{r}_{p,k} = G_k/(4\pi r_{p,k}^2 \rho_{\text{dens}})$, where ρ_{dens} denotes the mass density of the solid pellet material. The factor f_{ij} denotes the particle fraction of the ablated material that is deposited to n_{ij}. The pellet molar mass is denoted by $\mathcal{M}$, and N_{A} is the Avogadro number. The radial distribution of the homogenized density increase is described by the factor $H(r, \rho_{p,k}) = h(r, \rho_{p,k})/A_{\text{fls}}(r)$, where $h(r, \rho_{p,k})\mathrm{d}r$ describes the fraction of the material deposited at a radius between r and $r + \mathrm{d}r$ ablated from a pellet at radius $\rho_{p,k}$. Here, A_{fls} is the area of the flux surface at radius r.

For the SPI simulations presented in this work, the mass ablation rates G_k are calculated using the NGS model given by equations (3.2) and (3.3), and the initial shard sizes are drawn from the distribution given by equation (3.1). As a first approximation, the pellet shards may be assumed to travel along straight lines starting from a point close to the tokamak wall, following specified angular and speed distributions.

The most realistic model for the charge state distribution of the newly ablated material is to add it to the neutral charge state of the relevant species. However, at the relatively high plasma temperatures into which the pellets are injected, the fast ionization process of the lower charge states might introduce a problematic bottleneck in the need for time resolution. To circumvent this issue, one may deposit the ablated material directly to the equilibrium distribution of charge states associated with the local density and temperature, which can be found by solving equation (4.1) with the time derivative set to zero.

The width of the volume within which the ablated material is deposited may be approximated by the width of the shielding cloud around the pellet, with a radius $r_{\text{cld}} \sim 1$ cm. However, in some cases, one might be required by computational feasibility to have a radial cell size that is significantly larger than such a width of the pellet cloud, and the radial resolution then becomes the limiting length scale for the spread of the ablated material. In such cases, it is more reasonable to use a delta function deposition kernel, $h = \delta(r - \rho_{p,k})$ which, when discretized in time, translates to a uniform distribution over the distance traveled during the current time step. The deposition kernel can also be shifted compared to the pellet position to account for the cross-field drift of the ablated material described in section 3.4.1, e.g. using the model derived in paper **D**. However, the SPI studies performed in paper **C** of this work neglect this effect, as no sufficiently accurate and computationally efficient model was available at the time of writing.

A more detailed description of the SPI model available in the DREAM code is given in paper **C**.

4.2 Plasma cooling

When the cold pellet material is deposited, the hot plasma is initially cooled simply by dilution of the thermal energy on the local flux surface over the new particles. Thereafter, the partially ionized particles in the deposited material dissipate the thermal energy as radiation, either directly through line radiation or indirectly by ionization, resulting in a final radiative loss during recombination. Moreover, the

introduction of high-Z impurities is expected to trigger or accelerate the growth of MHD instabilities resulting in a stochastisation of the magnetic field. This stochastisation increases the transport of thermal energy out of the plasma during the early parts of the disruption, as discussed in section 1.2, before the flux surfaces re-heal when the thermal quench approaches its end. The thermal energy is also affected by local Ohmic heating from the thermal part of the plasma current and, at high temperatures, bremsstrahlung losses.

We now turn to the model used for the evolution of the temperature and energy density of the Maxwellian bulk of electrons, $W_\mathrm{M} = 3n_\mathrm{M}T_\mathrm{M}/2$. The part of the electron distribution function deviating from a Maxwellian is treated separately later in section 4.3. The transport of thermal energy along the stochastic magnetic field lines is expected to result in an exponential-like decay of the temperature. Thus, as a simple first approximation, one may prescribe an exponential temperature evolution from temperature $T_0(r)$ to $T_\mathrm{final}(r)$,

$$T_\mathrm{M} = T_\mathrm{final} - (T_\mathrm{final} - T_0)e^{-t/t_\mathrm{TQ}}, \tag{4.4}$$

with the characteristic thermal quench time $t_\mathrm{TQ} \sim 1$ ms.

The exponential decay model may be useful for making a first, computationally efficient, exploration of a new scenario. However, many important aspects of the interaction between the injected material and the background plasma occur via its effect on the temperature, which is not resolved by this model. Resolving these effects require a self-consistent treatment of the energy balance in the plasma, which can be expressed as

$$\begin{aligned}\frac{\partial W_\mathrm{M}}{\partial t} = \frac{3n_\mathrm{M}}{2r}\frac{\partial}{\partial r}\left[rD_W\frac{\partial T_\mathrm{M}}{\partial r}\right] - \left(\frac{\partial W_\mathrm{M}}{\partial t}\right)_\mathrm{line} - \left(\frac{\partial W_\mathrm{M}}{\partial t}\right)_\mathrm{ioniz} + \left(\frac{\partial W_\mathrm{M}}{\partial t}\right)_\mathrm{Ohm} \\ + \left(\frac{\partial W_\mathrm{M}}{\partial t}\right)_\mathrm{col} + \left(\frac{\partial W_\mathrm{M}}{\partial t}\right)_\mathrm{brems} + \left(\frac{\partial W_\mathrm{M}}{\partial t}\right)_\mathrm{ioniz}^\mathrm{abl},\end{aligned} \tag{4.5}$$

where the first four terms typically dominate the evolution of the energy density. The dilution effect is captured by the fact that an increase in the thermal electron density n_M must be compensated by a drop in the temperature T_M to maintain a given energy density W_M.

The first term in equation (4.5) describes a diffusive energy transport due to magnetic perturbations. When electrons follow stochastically perturbed magnetic field lines, their radial dynamics may be approximated as a diffusion process. In a tokamak geometry, a heuristic argument gives the Rechester-Rosenbluth form for the radial diffusion coefficient, $D = \pi q\left|v_{||}\right|R_\mathrm{m}\left(\delta B/B\right)^2$ (Rechester & Rosenbluth, 1978), for a particle traveling with a speed $v_{||}$ along the field lines. The factor πqR_m represents the parallel correlation length scale of the stochastic magnetic field perturbation, and $\delta B/B$ is the relative amplitude of the perturbation. The local electron heat diffusion coefficient D_W is calculated by integrating the diffusion coefficient D over a Maxwellian with the local temperature T_M:

$$D_W = \frac{1}{\pi^{3/2}v_T^3T_\mathrm{M}}\int\frac{m_ev^2}{2}\left(\frac{v^2}{v_T^2} - \frac{3}{2}\right)D(\boldsymbol{v})\exp\left(-\frac{v^2}{v_T^2}\right)\mathrm{d}\boldsymbol{v}, \tag{4.6}$$

where $v_T = \sqrt{2T_\mathrm{M}/m_e}$ is the electron thermal velocity. Lacking a self-consistent model, the evolution of $\delta B/B$ is prescribed in our simulations. When studying ITER-like scenarios, we typically set $\delta B/B$ to the order of 10^{-3} until the end of the thermal quench, after which it is set to zero. This value results in a transport loss time scale $\sim a^2/D_W$, with D_W evaluated at the initial temperature, of the same order of magnitude as the expected thermal quench time in ITER (Breizman *et al.*, 2019).

The transport term often dominates at the high initial temperature during a disruption, but due to the temperature scaling of the various loss mechanisms, the transport typically becomes subdominant to the radiation and ionization losses, described by the second and third term of equation (4.5), respectively, at temperatures $\lesssim 100$ eV. These terms can be expressed as

$$\left(\frac{\partial W_\mathrm{M}}{\partial t}\right)_\mathrm{line} = n_\mathrm{M} \sum_{ij} n_{ij} L_{ij}(T_\mathrm{M},\, n_\mathrm{M}) \tag{4.7}$$

and

$$\left(\frac{\partial W_\mathrm{M}}{\partial t}\right)_\mathrm{ioniz} = n_\mathrm{M} \sum_{ij} n_{ij} E_{ij}^\mathrm{ioniz} I_{ij}(T_\mathrm{M},\, n_\mathrm{M}), \tag{4.8}$$

where the line radiation rates L_{ij} are taken from the ADAS-database in a similar fashion to the ionization and recombination rates, and the ionization energies E_{ij}^ioniz are taken from the NIST database[‡]. Note that ionization losses are still present when the net electron density does not increase, as in that case the ionization and recombination processes are still active although they balance each other. At temperatures in the few eV range, the line radiation and ionization losses are balanced by the Ohmic heating, preventing the temperature from dropping further. The Ohmic heating is given by

$$\left(\frac{\partial W_\mathrm{M}}{\partial t}\right)_\mathrm{Ohm} = \sigma_{||} E_{||}^2, \tag{4.9}$$

where $\sigma_{||}$ is the plasma conductivity and $E_{||}$ is the electric field parallel to the magnetic field lines.

The last three terms in equation (4.5) correspond to the collisional energy exchange between the non-Maxwellian electron population and the bulk, bremsstrahlung losses, and ionization energy required for the initial ionization of the ablated material (in case the ablated material is deposited directly to an ionized charge state), respectively. These contributions typically play a rather minor role in a disruption, but are included to obtain a more accurate energy conservation. A more detailed description of the terms in equation (4.5) is given by Hoppe, Embreus & Fülöp (2021), and a more detailed summary is also given in appendix A of paper **C**.

4.3 Electric field and currents

The rapid cooling of the plasma is accompanied by a rapid drop in the conductivity, resulting in the induction of an electric field, that later decays in a diffusive

[‡]`https://physics.nist.gov/PhysRefData/ASD/ionEnergy.html`

manner. Combining the Faraday induction law and Ampere's law (disregarding the displacement current which is not relevant on the time scales of interest here) yields

$$\mu_0 \frac{\partial j_{||}}{\partial t} = \nabla^2 E_{||}, \tag{4.10}$$

where $j_{||}$ denotes the total current density parallel to the field lines. This current density is comprised of the sum of the contribution from the Ohmic current carried by the thermal bulk of electrons, and the contribution from the more energetic, superthermal electrons, including the runaway electrons, which are treated separately in our model.

As a relatively simple, and thus computationally efficient, approximation, we separate the electron population into a thermal (Maxwellian) population, which carries the Ohmic current density $j_{\mathrm{Ohm}} = \sigma_{||} E_{||}$, and a runaway population characterized by the number density n_{RE} that is assumed to travel at the speed of light parallel to the field lines. The runaway population thus carries the current density $j_{\mathrm{RE}} = ecn_{\mathrm{RE}}$. The time evolution of the runaway population is determined by analytical approximations of the total flux of electrons into the runaway region of momentum space due to the various mechanisms introduced in section 2.2.2. An overview of the corresponding source terms are given below, referring to paper **B** for a more detailed summary.

For the tritium decay and Compton scattering sources, this flux can be calculated by directly integrating the corresponding source terms over the runaway region of momentum space. The runaway seed produced by tritium decay then becomes (Martín-Solís, Loarte & Lehnen (2017), Paper **A**)

$$\left(\frac{\partial n_{\mathrm{RE}}}{\partial t}\right)^{\mathrm{tritium}} = \ln(2) \frac{n_{\mathrm{T}}}{\tau_{\mathrm{T}}} f\left(W_{\mathrm{crit}}\right), \tag{4.11}$$

where n_{T} is the tritium density, $\tau_{\mathrm{T}} \approx 4500$ days is the half-life of tritium. The fraction of the electrons created by tritium β^- decay above the critical runaway energy W_{crit} is given by $f(W_{\mathrm{crit}}) \approx 1 - (35/8)w^{3/2} + (21/4)w^{5/2} - (15/8)w^{7/2}$, with $w = W_{\mathrm{crit}}/Q$ and $Q = 18.6\,\mathrm{keV}$, corresponding to the maximum energy of the β^- electrons.

Runaway generation due to Compton scattering of gamma photons from the activated wall takes the form

$$\left(\frac{\partial n_{\mathrm{RE}}}{\partial t}\right)^{\gamma} = n_{\mathrm{tot}} \int \Gamma_\gamma(E_\gamma)\sigma(E_\gamma) dE_\gamma, \tag{4.12}$$

where $\Gamma(E_\gamma)$ is the gamma photon energy spectrum and $\sigma(E_\gamma)$ is the total Compton scattering cross-section as a function of the gamma photon energy E_γ (Martín-Solís, Loarte & Lehnen, 2017). The gamma photon energy spectrum depends on the details of the geometry and irradiation of the tokamak wall, and therefore varies between different machines. An estimated spectrum for ITER, which is of most interest in this work, obtained using radiation transport calculations performed at several poloidal locations, is available in Martín-Solís, Loarte & Lehnen (2017). The dependence on n_{tot}, rather than the free electron density, reflects the fact that the

gamma photon energies are much larger than the ionization energies of the ions and atoms in the plasma. Thus, the bound electrons may be scattered into the runaway momentum region essentially to the same extent as the free electrons.

The calculation of the remaining runaway sources requires an approximate analytical or numerical solution to the kinetic equation introduced in section 2.2. As the relatively cold post-thermal quench plasma may contain a substantial fraction of partially ionized ions and atoms, the collision frequencies must account for the presence of both free and bound electrons, as well as the partial screening of the nuclei surrounded by bound electrons (Hesslow *et al.*, 2018*a*). For the Dreicer mechanism, this is done by using a neural network trained on output from kinetic simulations (Paper **F**).

The growth rate for the avalanche process is calculated based on an asymptotic matching of solutions to the kinetic equation in various limits, and is given by (Paper **E**)

$$\left(\frac{\partial n_{\mathrm{RE}}}{\partial t}\right)^{\mathrm{avalanche}} = \frac{e n_{\mathrm{RE}}}{m_{\mathrm{e}} c \ln\Lambda_{\mathrm{c}}} \frac{n_{\mathrm{tot}}}{n_{\mathrm{M}}} \frac{E_{||} - E_{\mathrm{c}}^{\mathrm{eff}}}{\sqrt{4 + \bar{\nu}_{\mathrm{S}}(\bar{p}_\star)\bar{\nu}_{\mathrm{D}}(\bar{p}_\star)}}, \tag{4.13}$$

where $E_{\mathrm{c}}^{\mathrm{eff}}$ is the effective critical electric field taking into account screening effects, as well as bremsstrahlung and synchrotron radiation losses due to the gyro-motion of the electrons, which were not accounted for in the expression introduced in section 2.2.2. An accurate expression for $E_{\mathrm{c}}^{\mathrm{eff}}$ was derived by Hesslow *et al.* (2018*b*). The normalized deflection and slowing-down frequencies $\bar{\nu}_{\mathrm{D}}$ and $\bar{\nu}_{\mathrm{S}}$, respectively, with partial screening effects taken into account, are given by Hesslow *et al.* (2018*a*). The factor $n_{\mathrm{tot}}/n_{\mathrm{M}}$ reflects the fact that the runaway electrons typically reach energies much higher than the ionization potential of the bound electrons, making them available as target electrons for the avalanche process, while they do not contribute to the frictional drag to the same extent as free electrons for $E_{||} \gg E_{\mathrm{c}}^{\mathrm{eff}}$. Thus, the avalanche growth rate typically increases with an increased ratio of bound electrons.

The above runaway generation mechanisms are typically captured with sufficient accuracy by the analytical growth rates given above, without needing to resolve any further details of the electron momentum distribution function. However, in order to accurately capture the hot-tail mechanism, which is an intrinsically transient phenomenon sensitive to the details of the electron distribution function, it is necessary to solve the kinetic equation self-consistently with the temperature evolution for at least a part of the momentum space[§].

In order to do this in a computationally efficient manner, we treat the Maxwellian electrons and the superthermal electrons separately. The separation is made by introducing a momentum p_{hot}, and considering electrons with a momentum larger than $p_{\mathrm{hot}} \sim 10 p_{\mathrm{th}}$, as superthermal, where p_{th} is the thermal momentum. To further increase the computational efficiency, we also divide the superthermal electrons into two parts referred to as the hot population and the runaway population, respectively, separated by a momentum $p_{\mathrm{RE}} \sim m_{\mathrm{e}} c$. The hot population is characterized by the part f_{hot} of the distribution function with $p_{\mathrm{hot}} < p < p_{\mathrm{RE}}$, while the runaway

[§]It should however be mentioned that it is possible to approximately account for the hot-tail mechanism using an analytical growth rate similar to the above, which might be sufficiently accurate in some situations (Hoppe, Embreus & Fülöp, 2021; Smith & Verwichte, 2008).

electrons are again characterized by a density n_{RE}, and are approximated to travel with the speed of light, as above.

Using the above division of the momentum space, we resolve the part of momentum space with $p < p_{\mathrm{RE}}$ by solving the gyro-averaged kinetic equation with a linearized relativistic test particle Coulomb Fokker-Planck collision operator, introduced in section 2.2.1. The reference Maxwellian around which this collision operator is linearised is defined by the density n_{M} and temperature T_{M}, as calculated by equations (4.5) and (4.1), and the quasi-neutrality condition, with n_{M} defined as the density of electrons with $p < p_{\mathrm{hot}}$. As the kinetic equation is invoked here to study the comparatively small non-Maxwellian population, while the Maxwellian population is evolved by equations (4.5) and (4.1), the field particle term in equation (2.12) is omitted. In addition to the test particle collision operator, in case any magnetic perturbations are included in the scenario to be modeled, we include a diffusive radial transport term with the Rechester-Rosenbluth form of the diffusion coefficient, as introduced for the thermal energy density in section 4.2. The slowing down and deflection frequencies in the test particle operator are taken to be those accounting for the energy dependence of the Coulomb logarithm, as well as the effect of partial screening in collisions with partially ionized impurities, as derived by Hesslow *et al.* (2018*a*). Using the coordinates p and ξ, where p is the magnitude of the momentum and ξ is the cosine of the pitch angle, this kinetic equation reads

$$\frac{\partial f}{\partial t} + eE\left(\frac{1}{p^2}\frac{\partial}{\partial p}\left[p^2\xi f\right] + \frac{1}{p}\frac{\partial}{\partial \xi}\left[\left(1-\xi^2\right) f\right]\right) = \frac{1}{p^2}\frac{\partial}{\partial p}\left[p^3\nu_s f\right] + \frac{\nu_D}{2}\frac{\partial}{\partial \xi}\left[(1-\xi^2)\frac{\partial f}{\partial \xi}\right] + \frac{1}{r}\frac{\partial}{\partial r}\left[rD\frac{\partial f}{\partial r}\right] + S\delta(\boldsymbol{p}), \tag{4.14}$$

where we neglect the collisional energy-diffusion term, an assumption strictly valid in the superthermal limit. The strength S of the delta function source term at $\boldsymbol{p} = 0$ is determined by the requirement that the total number of particles on the kinetic grid must satisfy quasi-neutrality, $\int f(\boldsymbol{p})d\boldsymbol{p} = n_{\mathrm{free}} - n_{\mathrm{RE}}$.

The solution to equation (4.14) is then used to calculate the current density j_{hot} carried by the hot population and momentum space flux F_{p} across the upper boundary p_{RE}, which then corresponds to the sum of the hot-tail and Dreicer runaway generation mechanisms. A diffusion term of the Rechester-Rosenbluth form is also added for the runaway density n_{RE}, with $v_{||} = c$, in case any magnetic perturbations are included in the scenario of interest. Finally, the total current density can then be expressed as $j_{||} = E_{||}\sigma_{||} + j_{\mathrm{hot}} + ecn_{\mathrm{RE}}$, with the time evolution of the runaway population determined by

$$\frac{\partial n_{\mathrm{RE}}}{\partial t} = F_p + \left(\frac{\partial n_{\mathrm{RE}}}{\partial t}\right)^{\mathrm{Dreicer}} + \left(\frac{\partial n_{\mathrm{RE}}}{\partial t}\right)^{\mathrm{tritium}} + \left(\frac{\partial n_{\mathrm{RE}}}{\partial t}\right)^{\gamma} + \left(\frac{\partial n_{\mathrm{RE}}}{\partial t}\right)^{\mathrm{avalanche}} + \frac{1}{r}\frac{\partial}{\partial r}\left[rD\frac{\partial n_{\mathrm{RE}}}{\partial r}\right]. \tag{4.15}$$

4.4 Numerical tools

Having described our model from a physics point of view, we here give a brief overview of the numerical tools GO (Fehér *et al.* (2011), paper **B**) and DREAM (Disruption Runaway Electron Analysis Model) (Hoppe, Embreus & Fülöp, 2021) used for the numerical studies in papers **A**-**B** and paper **C**, respectively. Based on an input specifying the injection parameters and pre-disruption plasma conditions, both codes are capable of self-consistently calculating the time evolution of the background plasma properties, the runaway current and, for the DREAM code, the electron momentum distribution function, during a mitigated tokamak disruption.

The GO code is a purely fluid model, in the sense that it does not resolve any details of the electron momentum distribution function, but merely treats a thermal population assumed to have a Maxwellian momentum distribution and a runaway population assumed to travel with the speed of light. Thus, we do not use the GO code to study the hot-tail mechanism in this work. The evolution of the total (i.e. sum of all charge states) ion density of the injected material is directly prescribed by the user. The radial discretization is made using the finite difference method, with the radial derivatives calculated using the central approximation. The time stepping is performed using the Crank-Nicholson scheme for the electric field diffusion equation (4.10) and the diffusion term in the runaway density equation (4.15), while for the other terms it is performed using the Euler forward scheme. With its relatively simple and modular design, the code is well suited to quickly implement and explore new components of the disruption model.

In addition to the modeling capabilities of the GO code, the DREAM code also offers the possibility to solve for the electron momentum distribution function, making it more suitable for studies of e.g. the hot-tail runaway generation mechanism where such information is needed. Moreover, in paper **C**, the DREAM code was extended with the capability of modeling an SPI with input parameters specifying the size, composition and shattering of the pellet and the velocity distribution of the shards, instead of simply prescribing the evolution of the total injected density.

The equation system in DREAM is discretized using a finite volume method (see e.g. Karney (1986)) for the momentum and configuration space, and an Euler backward scheme for the time. Approximating the derivatives with central differences, the differential equations included in the model are translated into an algebraic equation system for the cell averages of the various quantities at the next time step. The evolved quantities are thus computed in the center of the cells, while the fluxes between adjacent cells are calculated on the cell surfaces, ensuring that the flux into a grid cell exactly equals the flux out of adjacent grid cells. This guarantees conservation of the integrals of the various quantities to within machine precision, in the absence of sources and edge losses, thus satisfying the physical conservation laws of e.g. particle number and energy. The interpolation from the center of the cells to the cell boundaries, needed for the calculation of the fluxes, is performed in such a way as to preserve positivity of the evolved quantities.

The implicit solution for the evolved quantities in the next time step is obtained via Newton iteration, using a Jacobian constructed based on analytical derivatives, although some are approximated or even neglected to limit the complexity of the

construction and inversion of the Jacobian. The iteration starts at the vector containing all the evolved quantities in the previous time-step, and continues until a tolerance specified by the user is satisfied separately for every evolved quantity.

Chapter 5

Summary and outlook

Disruptions are a severe threat to the future of fusion energy based on the tokamak design. A reliable disruption mitigation system is of utmost importance for the success of future large, high-current devices such as ITER. The currently envisaged method of mitigation is to inject massive amounts of material into the plasma, aiming to rapidly cool the plasma in a controlled way. The injected material can be delivered in a variety of ways, such as in the form of a gas released from a pressurized vault or in the form of a Shattered Pellet Injection (SPI), with the latter being chosen as the basis for the ITER disruption mitigation system. The objectives of the disruption mitigation system concern three main issues related to disruptions: mitigation of the localized heat loads and electromagnetic forces on the vessel, and the reduction of the runaway current generation. The mitigation of the localized heat loads is achieved by isotropically dissipating the thermal energy content through radiation. To avoid excessive electromagnetic forces, the current quench time must be long enough to sufficiently reduce the eddy currents induced in the structures surrounding the plasma, but short enough to avoid excessive halo currents. Finally, the runaway current must be sufficiently low to avoid substantial damage upon wall impact.

To achieve these goals, a detailed understanding and modeling capability of tokamak disruptions mitigated by massive material injection is crucial in order to guide the design and operation of the disruption mitigation system. This is the topic to which this thesis aims to contribute. This chapter summarizes the main findings of the attached papers in section 5.1, along with a summary of the most critical remaining questions to be addressed and suggestions for future research in section 5.2.

5.1 Summary of papers

In papers **A**-**C**, we perform numerical simulations of tokamak disruptions and their mitigation by massive material injection, considering increasingly advanced scenarios and physics fidelity. Paper **A** presents a derivation of the electric field diffusion equation (4.10) for a large aspect ratio tokamak with flux surfaces having elliptical cross section. This equation is then implemented in the GO code, extending the beyond purely cylindrical flux surfaces. The updated GO code is then used to study

the impact of the elongation of the flux surfaces on the current dynamics during an unmitigated tokamak disruption, considering a prescribed exponential temperature decay, scanning over a wide range of decay time scales and post-thermal quench temperatures. This study is performed for both the ITER and SPARC tokamaks, thus also providing a comparison of the current dynamics during a disruption for two different reactor-relevant tokamak designs, with the most important differences being the different sizes and plasma currents. The runaway generation mechanisms considered include the Dreicer mechanism, the contribution from the tritium decay, and the avalanche mechanism. The hot-tail mechanism is disregarded due to the lack of a computationally efficient kinetic solver. The contribution from the Compton scattering of gamma photons from the activated wall is also neglected as the necessary data on the gamma spectrum in the SPARC tokamak was not available. Similarly, the radial losses of runaway electrons due to the stochastic magnetic field was neglected due to the lack of the necessary data for the magnetic field perturbation level.

We find that elongated plasmas generally produce lower runaway currents compared to cylindrical plasmas. This happens partly due to direct shaping effects, but mostly due to the lower induced electric fields needed to drive a given total plasma current within the larger plasma cross section of an elongated plasma. This effect is most pronounced for the SPARC tokamak, in which the main contribution to the runaway electron seed is generated by the Dreicer mechanism when the system is approximated as cylindrical. As the Dreicer mechanism is exponentially sensitive to the electric field, the reduction of the electric field due to the larger plasma cross section of the elongated plasma was found to effectively reduce the Dreicer seed to a negligible level compared to the seed generated by the tritium decay. This also resulted in an order unity, but still significant, reduction of the final runaway current after the avalanche amplification. The final runaway currents were found to be rather small, of the order of a few percent of the initial plasma current of 7.5 MA, unless the temperature drop is extremely rapid and the final temperature becomes less than a few eV.

For ITER, on the other hand, the Dreicer mechanism was found to be negligible with both the cylindrical and elongated geometry. The runaway current is instead determined by the contribution from the tritium decay, which is then strongly amplified by the avalanche mechanism. The contribution from the tritium decay is insensitive to the electric field once W_{crit} becomes small compared to Q, which happens when for $E_{\parallel} \gtrsim 10E_{\mathrm{c}}$, and the avalanche mechanism is linearly dependent on the electric field. With these comparatively weak sensitivities to the electric field, the effect of the reduction of the electric field is largely compensated by the increase in the electric field diffusion time resulting from the larger plasma cross section of the elongated geometry, leaving only a $\lesssim 10\,\%$ reduction of the runaway current due to the direct shaping effects. The runaway currents were in general found to be significantly larger in ITER compared to SPARC, with values of about 1-2 MA ($\sim 10\%$ of the initial plasma current of 15 MA). Notably, this is significantly larger than the ~ 0.15 MA expected to be tolerable in ITER(Lehnen & the ITER DMS task force, 2021).

In paper **B**, we continue performing GO simulations of disruptions in deuterium-

tritium plasmas in ITER, now mitigated by the injection of a mixture of deuterium and neon or argon, evaluating the current quench time and runaway current generated for a wide range of injected densities. The initial part of the temperature drop, where the transport due to the stochastization of the magnetic field is expected to play a major role, is modeled by an exponential decay down to ~ 100 eV. After this, the energy balance is calculated self-consistently, assuming that it is dominated by radiation and Ohmic heating. The injected material is assumed to be instantly deposited in the neutral state with a homogeneous density profile at $t = 0$, after which the ionization and recombination processes are calculated self-consistently. In addition to the runaway generation mechanisms included in papaer A, here we also account for the Compton scattering of gamma photons from the activated wall, using the model presented by Martín-Solís, Loarte & Lehnen (2017), while still disregarding the hot-tail mechanism. One of the main objectives of the paper was to study how the runaway generation is affected by the partial screening of the partially ionized ions and atoms present in the cold post-disruption plasma. This is done using the newly implemented models accounting for these effects on the Dreicer and avalanche mechanisms, which were first demonstrated in papers **F** and **E**, respectively.

We find that the partial screening substantially increases the runaway generation, compared to the results obtained assuming a complete screening of the nuclei carrying bound electrons. This is explained by the shift in the balance between the frictional drag and contribution to the number of target electrons for the avalanche mechanism in the presence of bound electrons, as discussed in section 4.3. The increase can be counteracted to some extent by combining the neon or argon injection with a large amount of deuterium, which stays ionized at lower temperatures and thus reduces the fraction of bound electrons. However, when the injected quantities become large enough, the temperature starts to drop as low as ~ 1 eV already when there is a significant Ohmic current left in the plasma. When this happens, the deuterium also starts to recombine, which substantially increases the avalanche generation, converting a significant fraction of the remaining Ohmic current into a runaway current. At this point, the runaway current starts to increase with an increased amount of injected deuterium. Moreover, if the injected quantities are too low, the radiative cooling is found to be insufficient to cause a complete thermal quench, leaving the equilibrium temperature in the ~ 100 eV range. This results in a high post-thermal quench plasma conductivity and thus a too long current quench time. With the present model, the lowest runaway current found, within the range of injection parameters also giving an acceptable current quench time, was 3.7 MA.

The physics fidelity is further increased in paper **C**, where we use the recently developed DREAM code to study mitigated ITER disruptions, including a kinetic calculation of the hot-tail runaway generation. For this paper, we also equipped the DREAM code with an SPI model, allowing for a self-consistent calculation of the assimilation of the injected material in such injections. Moreover, all parts of the temperature drop are now calculated self-consistently, with the transport due to the stochastization of the magnetic field accounted for by a diffusion term of the Rechester-Rosenbluth form, as described in section 4.2. A major advantage of this model compared to prescribing an exponential temperature drop for the

relevant part of the disruption is that it makes it possible to estimate the fraction of the thermal energy lost by transport, which can be used as a measure of the performance concerning the mitigation of localized heat loads. However, to avoid the computational complexity introduced by transporting particles between the radial grid points on the kinetic grid, the radial transport of the superthermal electrons is still neglected, and thus the calculated runaway currents should be interpreted as upper estimates. Finally, the line radiation and ionization/recombination model is updated to account for the opacity to the resonant Lyman lines of the hydrogen species expected at large injected deuterium densities. With these updates included, the main purpose of this paper is to evaluate the performance of the two-stage SPI mitigation scheme recently suggested for ITER, described in section 3.1.

The two-stage injection scheme was found to significantly impede the thermal energy transport due to magnetic perturbations, which can reduce localized heat loads. This is explained by the decrease in the thermal motion due to the dilution cooling in the first stage, before the stochastization of the magnetic field, which effectively reduces the cross-field transport possible along the stochastic magnetic field lines. Moreover, this injection scheme was found to effectively reduce the hot-tail runaway seed generation by several orders of magnitude. This reduction can be explained by the intermediate equilibration of the hot tail of the electron momentum distribution between the injections, as discussed in section 3.1. Notably, this strong reduction was obtained despite the conservative assumption that the superthermal electrons were not affected by the magnetic field perturbations.

For the final runaway current, a non-monotonic dependence on the injected deuterium density similar to that observed in paper **B** was also found here. However, the opacity to Lyman radiation was found to significantly reduce the cooling at temperatures $\lesssim 2$ eV, resulting in a shift of the deuterium recombination, and the related enhancement of the runaway avalanche, towards higher injected densities. For a non-nuclear plasma, i.e. in the absence of runaway generation due to tritium decay and Compton scattering, when accounting for opacity to Lyman radiation, the runaway current was found to be below the acceptable limit when injecting a deuterium pellet containing $\gtrsim 10^{24}$ atoms, with a rather weak dependence on the amount of injected neon in the range of $10^{22} - 10^{25}$ atoms. For activated operation, on the other hand, no such scenarios were found, and the lowest runaway currents found (again, within the range of injection parameters also giving an acceptable current quench time) were in the 3-4 MA range, similar to the results of paper **B**.

Despite the relatively high physics fidelity of paper **C**, a number of effects remain to be addressed. One such effect is the cross-field drift of the ablated pellet material, introduced in section 3.4.1. Accounting for this effect in a study similar to that of paper **C** would require a computationally efficient, preferably analytical, model for the total shift of the ablation material, as a function of the pellet and background plasma parameters, accounting for all the mechanisms regulating the drift introduced in section 3.4.1. Such a model was, to our knowledge, not available in the literature, and the derivation of such a model is therefore the subject of paper **D**. In paper **D**, we present a detailed derivation of the current balance equation governing the motion of an ablation plasmoid, along with an analytical solution assuming an approximate model of the plasmoid expansion parallel to the field lines. One of the main novelties

included is a statistical model for the field lines connecting the toroidally opposite sides of the plasmoid, and the corresponding Ohmic current flowing along those field lines, thus avoiding the need to numerically calculate the detailed paths of the field lines.

This model is then applied to determine the extent of the expected drift in an ITER-relevant scenario, for a variety of pellet compositions. The results indicate that material ablated from a pure deuterium pellet is likely to drift a distance similar to the plasma minor radius, i.e. a substantial part of the material is likely to be completely ejected from the plasma. The evaluated drift distance was however found to be significantly reduced when adding a small amount of neon to the pellet, whose radiation reduces the temperature, and thus the excess pressure, inside the drifting plasmoid. This suggests that one should add a small amount of neon also to the first stage of the two-stage SPI scheme studied in paper **C**. The consequences of slightly doping the first pellet, in particular its effect on the MHD stability of the plasma, should however be studied further before implementation.

5.2 Outlook

The seriousness of the disruption issue for future reactor-scale tokamaks, which is further corroborated by the results summarized above, highlights the importance of further disruption mitigation studies, and motivate the development of models with a more rigorous treatment of the most simplified aspects of the present model. While the model used in this work comprises an integrated framework accounting for many of the relevant aspects of disruption mitigation by massive material injection, the various aspects are treated with different levels of sophistication. The evolution of the current and, in the DREAM code, the momentum distribution of the electrons, are treated rigorously in the present model. On the other hand, some aspects of the transport properties of the thermal energy and plasma ions, as well as the evolution of the pellet material, are treated in a simplified manner.

One such simplification is the neglect of the cross-field drift of the ablated pellet material mentioned above. A natural next step regarding this issue is to implement the model derived in paper **D** in an integrated model such as DREAM, and assess its impact on the disruption mitigation performance. Such a study should also include the transport of ions after the deposition of the ablated material, as the radial particle transport associated with the large scale plasma instability during the thermal quench might to some extend cancel the initial outward shift due to the cross-field drift. Preferably, such a study should also assess the impact of adding a small amount of neon to the first injection stage of the two-stage SPI scheme, including the effect on the MHD stability of the plasma, although this would require a model for the magnetic field evolution beyond the capabilities of the DREAM code.

A second area of simplification employed in the present work concerns the geometry and interaction with the structures surrounding the plasma. The geometrical simplifications include the elliptical plasma cross section, neglect of the toroidicity and the assumption of flux surface homogenised quantities. Relaxing these assumptions would allow for modeling of transient 3D features of the plasma profiles, as well as introducing geometrical order unity corrections to the transport processes

involved. Regarding the surrounding structures, their geometry and conductive properties introduce corrections to the electric field boundary condition. Support for a shaped geometry (although still with constant plasma parameters over the flux surfaces) and a finite wall conductivity has recently been implemented in DREAM, and the sensitivity to these features could therefore be studied in the future.

A related simplification is the assumption that the flux surface geometry remains constant in time. In reality, the shape of the flux surfaces will vary in time, and the whole plasma is likely to drift substantially in the vertical direction during the time frame studied in this work. As the outermost flux surfaces reach the tokamak wall, the plasma will be scraped off in a transient manner, the details and timing of which might substantially affect the size of the runaway current and the severity of the loads actually imposed on the wall.

Finally, another simplification in the present model is the prescribed evolution of the magnetic perturbations. The prescribed magnetic perturbation is sufficient to study qualitative trends involving transport due to magnetic perturbations, as done in paper **C** of this work. However, self-consistent and quantitatively accurate simulations would require coupling to an MHD modeling code, such as JOREK Nardon *et al.* (2020*b*), for the evolution of the magnetic field. A major issue with such coupling is the typically significant amount of computational resource required. A full scale 3D simulation of a thermal quench with JOREK run on a large scale computing cluster takes of the order of months Nardon *et al.* (2020*a*). The thermal quench simulations with DREAM shown in this work, on the other hand, take at most up to a day on a desktop computer, when invoking the kinetic equation to calculate the hot-tail runaway generation. The run-times for pure fluid simulations with DREAM and GO, following through both the thermal and current quench, are no longer than a fraction of an hour.

The orders of magnitude lower computational expense of stand-alone simulations with DREAM substantially increases the feasibility of exploring a wide range of injection parameters. Instead of attempting a full scale coupling of the evolution of the fluid, kinetic and MHD properties of the plasma, a more feasible approach might be to use the output of a full scale MHD model such as JOREK to design a simplified MHD model. Such a model could then be efficiently integrated in a framework like the one used in this work, significantly improving the disruption modeling accuracy. Currently, coupling of the MHD, kinetic and fluid properties of the plasma might be one of the main questions remaining in order to make self-consistent, quantitatively accurate, predictions for the performance of disruption mitigation systems.

References

Baylor, L., Jernigan, T., Parks, P., Antar, G., Brooks, N., Combs, S., Fehling, D., Foust, C., Houlberg, W. & Schmidt, G. 2007 "Comparison of deuterium pellet injection from different locations on the DIII-D tokamak". *Nuclear Fusion* **47** (11), 1598–1606, DOI: 10.1088/0029-5515/47/11/023, URL https://doi.org/10.1088/0029-5515/47/11/023

Baylor, L., Combs, S., Foust, C., Jernigan, T., Meitner, S., Parks, P., Caughman, J., Fehling, D., Maruyama, S., Qualls, A., Rasmussen, D. & Thomas, C. 2009 "Pellet fuelling, ELM pacing and disruption mitigation technology development for ITER". *Nuclear Fusion* **49** (8), 085 013, DOI: 10.1088/0029-5515/49/8/085013, URL https://doi.org/10.1088/0029-5515/49/8/085013

Breizman, B. N., Aleynikov, P., Hollmann, E. M. & Lehnen, M. 2019 "Physics of runaway electrons in tokamaks". *Nuclear Fusion* **59** (8), 083 001, DOI: 10.1088/1741-4326/ab1822

Cabal, H., Lechon, Y., Bustreo, C., Gracceva, F., Biberacher, M., Ward, D., Dongiovanni, D. & Grohnheit, P. E. 2017 "Fusion power in a future low carbon global electricity system". *Energy Strategy Reviews* **15**, DOI: 10.1016/j.esr.2016.11.002

Chen, F. 1974 Introduction to Plasma Physics and Controlled Fusion. 1st edn., New York, NY, USA: Springer International Publishing

Chen, F. 2011 An indispensable truth: how fusion power can save the planet. New York, NY, USA: Springer Science & Business Media

Commaux, N., Pégourié, B., Baylor, L., Köchl, F., Parks, P., Jernigan, T., Géraud, A. & Nehme, H. 2010 "Influence of the low order rational q surfaces on the pellet deposition profile". *Nuclear Fusion* **50** (2), 025 011, DOI: 10.1088/0029-5515/50/2/025011, URL https://doi.org/10.1088/0029-5515/50/2/025011

Dreicer, H. 1959 "Electron and ion runaway in a fully ionized gas I". *Physical Review* **115** (2), 238, DOI: 10.1103/PhysRev.115.238

Embréus, O., Stahl, A. & Fülöp, T. 2016 "Effect of bremsstrahlung radiation emission on fast electrons in plasmas". *New Journal of Physics* **18** (9), 093 023

Embréus, O., Stahl, A. & Fülöp, T. 2018 "On the relativistic large-angle electron collision operator for runaway avalanches in plasmas". *Journal of Plasma Physics* **84** (1), 905840 102, DOI: 10.1017/S002237781700099X

Fehér, T., Smith, H. M., Fülöp, T. & Gál, K. 2011 "Simulation of runaway electron generation during plasma shutdown by impurity injection in ITER". *Plasma Physics and Controlled Fusion* **53** (3), 035 014, DOI: 10.1088/0741-3335/53/3/035014

Fontanilla, A. K. & Breizman, B. N. 2019 "Heating and ablation of high-z cryogenic pellets in high temperature plasmas". *Nuclear Fusion* **59** (9), 096 033, DOI: 10.1088/1741-4326/ab2bd6, URL https://dx.doi.org/10.1088/1741-4326/ab2bd6

Freidberg, J. P. 2008 Plasma physics and fusion energy. 1st edn., Cambridge, UK: Cambridge University Press

Helander, P. & Sigmar, D. 2005 Collisional Transport in Magnetized Plasmas. Cambridge, UK: Cambridge University Press

Hender, T., Wesley, J., Bialek, J., Bondeson, A., Boozer, A., Buttery, R., Garofalo, A., Goodman, T., Granetz, R., Gribov, Y., Gruber, O., Gryaznevich, M., Giruzzi, G., Günter, S., Hayashi, N., Helander, P., Hegna, C., Howell, D., Humphreys,

D., Huysmans, G., Hyatt, A., Isayama, A., Jardin, S., Kawano, Y., Kellman, A., Kessel, C., Koslowski, H., Haye, R. L., Lazzaro, E., Liu, Y., Lukash, V., Manickam, J., Medvedev, S., Mertens, V., Mirnov, S., Nakamura, Y., Navratil, G., Okabayashi, M., Ozeki, T., Paccagnella, R., Pautasso, G., Porcelli, F., Pustovitov, V., Riccardo, V., Sato, M., Sauter, O., Schaffer, M., Shimada, M., Sonato, P., Strait, E., Sugihara, M., Takechi, M., Turnbull, A., Westerhof, E., Whyte, D., Yoshino, R., Zohm, H., the ITPA MHD, D. & Group, M. C. T. 2007 "Chapter 3: MHD stability, operational limits and disruptions". *Nuclear Fusion* **47** (6), 128, doi: 10.1088/0029-5515/47/6/S03

Hesslow, L., Embréus, O., Hoppe, M., DuBois, T., Papp, G., Rahm, M. & Fülöp, T. 2018*a* "Generalized collision operator for fast electrons interacting with partially ionized impurities". *Journal of Plasma Physics* **84** (6), 905840605, doi: 10.1017/S0022377818001113

Hesslow, L., Embréus, O., Wilkie, G. J., Papp, G. & Fülöp, T. 2018*b* "Effect of partially ionized impurities and radiation on the effective critical electric field for runaway generation". *Plasma Physics and Controlled Fusion* **60** (7), 074010, doi: 10.1088/1361-6587/aac33e

Hirvijoki, E., Pusztai, I., Decker, J., Embréus, O., Stahl, A. & Fülöp, T. 2015 "Radiation reaction induced non-monotonic features in runaway electron distributions". *Journal of Plasma Physics* **81**, 475810502, doi: 10.1017/S0022377815000513/

Hollmann, E., Aleynikov, P., Fülöp, T., Humphreys, D., Izzo, V., Lehnen, M., Lukash, V., Papp, G., Pautasso, G., Saint-Laurent, F. *et al.* 2015 "Status of research toward the ITER disruption mitigation system". *Physics of Plasmas* **22** (2), 021802–1, doi: 10.1063/1.4901251

Hoppe, M., Embreus, O. & Fülöp, T. 2021 "DREAM: a fluid-kinetic framework for tokamak disruption runaway electron simulations". 2103.16457

Hu, D., Nardon, E., Lehnen, M., Huijsmans, G. & van Vugt and, D. 2018 "3D non-linear MHD simulation of the MHD response and density increase as a result of shattered pellet injection". *Nuclear Fusion* **58** (12), 126025, doi: 10.1088/1741-4326/aae614

ITER organization http://www.iter.org

Izzo, V., Hollmann, E., James, A., Yu, J., Humphreys, D., Lao, L., Parks, P., Sieck, P., Wesley, J., Granetz, R., Olynyk, G. & Whyte, D. 2011 "Runaway electron confinement modelling for rapid shutdown scenarios in diii-d, alcator c-mod and iter". *Nuclear Fusion* **51** (6), 063032, doi: 10.1088/0029-5515/51/6/063032, URL https://dx.doi.org/10.1088/0029-5515/51/6/063032

Karney, C. F. 1986 "Fokker-Planck and quasilinear codes". *Computer Physics Reports* **4** (3), 183, ISSN 0167-7977, doi: 10.1016/0167-7977(86)90029-8

Lang, P. T., Büchl, K., Kaufmann, M., Lang, R. S., Mertens, V., Müller, H. W. & Neuhauser, J. 1997 "High-efficiency plasma refuelling by pellet injection from the magnetic high-field side into ASDEX Upgrade". *Phys. Rev. Lett.* **79**, 1487–1490, doi: 10.1103/PhysRevLett.79.1487, URL https://link.aps.org/doi/10.1103/PhysRevLett.79.1487

Lehnen, M. & the ITER DMS task force 2021 "The ITER disruption mitigation system - design progress and design validation". https://tsdw.pppl.gov/Talks/2021/Lehnen.pdf. Presented at Theory and Simulation of Disruptions Workshop, PPPL

Lehnen, M., Jachmich, S., Kruezi, U. & the ITER DMS task force 2020 "The ITER disruption mitigation strategy". https://conferences.iaea.org/event/217/contributions/17867/. Presented by M. Lehnen at the IAEA Technical Meeting on Plasma Disruption and their Mitigation

Lengyel, L., Büchl, K., Pautasso, G., Ledl, L., Ushakov, A., Kalvin, S. & Veres, G. 1999 "Modelling of impurity pellet ablation in ASDEX Upgrade (neon) and Wendelstein W7-AS (carbon) by means of a radiative (`killer') pellet code". *Nuclear Fusion* **39** (6), 791, doi: 10.1088/0029-5515/39/6/307

MacAulay, A. 1994 "Geometrical, kinetic and atomic physics effects in a two dimensional time dependent fluid simulation of ablating fuel pellets". *Nuclear Fusion* **34** (1), 43, doi: 10.1088/0029-5515/34/1/i03

Martín-Solís, J. R., Loarte, A. & Lehnen, M. 2017 "Formation and termination of runaway beams in ITER disruptions". *Nuclear Fusion* **57** (6), 066 025, doi: 10.1088/1741-4326/aa6939

Matsuyama, A. 2022 "Neutral gas and plasma shielding (NGPS) model and cross-field motion of ablated material for hydrogen–neon mixed pellet injection". *Physics of Plasmas* **29** (4), 042 501, doi: 10.1063/5.0084586, URL https://doi.org/10.1063/5.0084586. https://doi.org/10.1063/5.0084586

Matsuyama, A., Nardon, E., Honda, M. & Lehnen, M. 2020 "ITER SPI modelling for runaway electron avoidance". https://ft.nephy.chalmers.se/?p=abstract&id=10. Presented at the 8th Runaway Electron Modelling (REM) meeting

Milora, S., Houlberg, W., Lengyel, L. & Mertens, V. 1995 "Pellet fuelling". *Nuclear Fusion* **35** (6), 657, doi: 10.1088/0029-5515/35/6/i04

Morozov, D., Gervids, V., Senichenkov, I., Veselova, I., Rozhansky, V. & Schneider, R. 2004 "Ionization–recombination processes and ablation cloud structure for a carbon pellet". *Nuclear Fusion* **44** (2), 252, doi: 10.1088/0029-5515/44/2/005

Mott, N. & Linfoot, E. 2006 A Theory of Fragmentation, (207). Berlin, Heidelberg: Springer Berlin Heidelberg, ISBN 978-3-540-27145-1, doi: 10.1007/978-3-540-27145-1_9

Nardon, E., Artola, J., Sommariva, C., Hoelzl, M., Hu, D. & Huijsmans, G. 2020*a* "JOREK simulations of MGI-triggered disruptions in JET". https://ft.nephy.chalmers.se/?p=abstract&id=11. Presented at the 8th Runaway Electron Modelling (REM) meeting

Nardon, E., Hu, D., Hoelzl, M. & and, D. B. 2020*b* "Fast plasma dilution in ITER with pure deuterium shattered pellet injection". *Nuclear Fusion* **60** (12), 126 040, doi: 10.1088/1741-4326/abb749

Nardon, E., Matsuyama, A. & Lehnen, M. 2020 "On the possible injection schemes with the ITER SPI system". https://conferences.iaea.org/event/217/contributions/16702/. Presented at the IAEA Technical Meeting on Plasma Disruption and their Mitigation

Papp, G., Pautasso, G., Decker, J., Gobbin, M., Mccarthy, P., Blanchard, P., Carnevale, D., Choi, D., Coda, S., Duval, B., Dux, R., Erdös, B., Esposito, B., Ficker, O., Fischer, R., Fuchs, C., Galperti, C., Giannone, L., Gude, A., Labit, B., Lackner, K., Lunt, T., Marelli, L., Martin, P., Mlynek, A., Maraschek, M., Marmillod, P., Nocente, M., Peysson, Y., Piovesan, P., Plyusnin, V., Pokol, G., Poloskei, P., Potzel, S., Reux, C., Saint-Laurent, F., Sauter, O., Sieglin, B., Sheikh, U., Sommariva, C., Suttrop, W., Tardini, G., Testa, D., Treutterer, W., Valisa, M., Team, T. & Team, E. M. 2016 "Runaway electron generation and mitigation on the european medium sized tokamaks ASDEX Upgrade and TCV". In "Proceedings of the 2016 IAEA Fusion Energy Conference",

Parks, P. 2016 "Modeling dynamic fracture of cryogenic pellets". Tech. Rep. GA-A28352, General Atomics, doi: 10.2172/1344852

Parks, P. 2017 "A theoretical model for the penetrationof a shattered-pellet debris plume". https://tsdw.pppl.gov/Talks/2017/Lexar/Wednesday%20Session%201/Parks.pdf. Presented at the Theory and Simulation of Disruptions Workshop

Parks, P. B. & Baylor, L. R. 2005 "Effect of parallel flows and toroidicity on cross-field transport of pellet ablation matter in tokamak plasmas". *Phys. Rev. Lett.* **94** (12), 125 002, doi: 10.1103/PhysRevLett.94.125002

Parks, P. B. & Turnbull, R. J. 1978 "Effect of transonic flow in the ablation cloud on the lifetime of a solid hydrogen pellet in a plasma". *The Physics of Fluids* **21** (10), 1735, doi: 10.1063/1.862088

Parks, P., Leffler, J. & Fisher, R. 1988 "Analysis of low Z impurity pellet ablation for fusion diagnostic studies". *Nuclear Fusion* **28** (3), 477, doi: 10.1088/0029-5515/28/3/012

Parks, P. B., Sessions, W. D. & Baylor, L. R. 2000 "Radial displacement of pellet ablation material in tokamaks due to the grad-b effect". *Physics of Plasmas* **7** (5), 1968, doi: 10.1063/1.874052

Pégourié, B. 2007 "Review: Pellet injection experiments and modelling". *Plasma Physics and*

Controlled Fusion **49** (8), 87, DOI: 10.1088/0741-3335/49/8/r01

Pegourie, B., Picchiottino, J.-M., Drawin, H.-W., Geraud, A. & Chatelier, M. 2002 "Pellet ablation studies on Tore Supra". *Nuclear Fusion* **33**, 591, DOI: 10.1088/0029-5515/33/4/I06

Pégourié, B., Waller, V., Nehme, H., Garzotti, L. & Géraud, A. 2006 "Homogenization of the pellet ablated material in tokamaks taking into account the ∇B-induced drift". *Nuclear Fusion* **47** (1), 44–56, DOI: 10.1088/0029-5515/47/1/006, URL https://doi.org/10.1088/0029-5515/47/1/006

Peherstorfer, T., Papp, G., Heinrich, P., de Marné, P., Dibon, M. & Jachmich, S. 2022 "Comparison of modeled and experimental SPI fragment sprays". https://ft.nephy.chalmers.se/?p=abstract&id=52. Presented at the 9th Runaway Electron Modelling (REM) meeting

Pégourié, B. & Picchiottino, J. 1996 "Plasma density buildup after pellet injection". *Physics of Plasmas* **3** (12), 4594, DOI: 10.1063/1.872030

Rechester, A. B. & Rosenbluth, M. N. 1978 "Electron heat transport in a tokamak with destroyed magnetic surfaces". *Phys. Rev. Lett.* **40**, 38, DOI: 10.1103/PhysRevLett.40.38

Reux, C., Plyusnin, V., Alper, B., Alves, D., Bazylev, B., Belonohy, E., Boboc, A., Brezinsek, S., Coffey, I., Decker, J., Drewelow, P., Devaux, S., de Vries, P., Fil, A., Gerasimov, S., Giacomelli, L., Jachmich, S., Khilkevitch, E., Kiptily, V., Koslowski, R., Kruezi, U., Lehnen, M., Lupelli, I., Lomas, P., Manzanares, A., Aguilera, A. M. D., Matthews, G., Mlynář, J., Nardon, E., Nilsson, E., von Thun, C. P., Riccardo, V., Saint-Laurent, F., Shevelev, A., Sips, G. & and, C. S. 2015 "Runaway electron beam generation and mitigation during disruptions at JET-ILW". *Nuclear Fusion* **55** (9), 093 013, DOI: 10.1088/0029-5515/55/9/093013

Rosenbluth, M. & Putvinski, S. 1997 "Theory for avalanche of runaway electrons in tokamaks". *Nuclear Fusion* **37** (10), 1355, DOI: 10.1088/0029-5515/37/10/i03

Rosenbluth, M. N., MacDonald, W. M. & Judd, D. L. 1957 "Fokker-planck equation for an inverse-square force". *Phys. Rev.* **107**, 1–6, DOI: 10.1103/PhysRev.107.1, URL https://link.aps.org/doi/10.1103/PhysRev.107.1

Rozhansky, V., Senichenkov, I., Veselova, I. & Schneider, R. 2004 "Mass deposition after pellet injection into a tokamak". *Plasma Physics and Controlled Fusion* **46** (4), 575–591, DOI: 10.1088/0741-3335/46/4/001, URL https://doi.org/10.1088/0741-3335/46/4/001

Shiraki, D., Herfindal, J., Baylor, L. R., Hollmann, E. M., Lasnier, C., Bykov, I., Eidietis, N., Raman, R., Sweeney, R., Sheikh, U., Gerasimov, S., Jachmich, S., Lehnen, M., Kim, J., Jang, J. J., Meitner, S. & Gebhart, T. 2020 "Particle assimilation during shattered pellet injection". https://conferences.iaea.org/event/217/contributions/16713/. Presented at the IAEA Technical Meeting on Plasma Disruption and their Mitigation

Smith, H. M. & Verwichte, E. 2008 "Hot tail runaway electron generation in tokamak disruptions". *Physics of Plasmas* **15** (7), 072 502, DOI: 10.1063/1.2949692

Smith, H., Helander, P., Eriksson, L.-G. & Fülöp, T. 2005 "Runaway electron generation in a cooling plasma". *Physics of Plasmas* **12** (12), 122 505, DOI: 10.1063/1.2148966

Sokolov, Y. A. 1979 ""multiplication" of accelerated electrons in a tokamak". *JETP Lett. (USSR) (Engl. Transl.); (United States)* **29** (4)

Summers, H. P. 2004 "The ADAS user manual, version 2.6". http://www.adas.ac.uk

UK Atomic Energy Authority https://step.ukaea.uk/

Vallhagen, O. 2021 "Disruption mitigation in tokamaks with shattered pellet injection". URL https://hdl.handle.net/20.500.12380/302296